Geophysical Journal International

Geophys. J. Int. (2024) **236,** 1545–1566
Advance Access publication 2023 December 30
GJI Rock and Mineral Physics, Rheology

https://doi.org/10.1093/gji/ggad500

Experimental study of seismic dispersion: influence of clay mineral content

K.S. Mews [1], S. Lozovyi,[2] J.F. Stenebråten,[2] S.B. Giger[3] and R.M Holt[1,2]

[1] *Department of Geoscience and Petroleum, Norwegian University of Science and Technology (NTNU),* 7491 *Trondheim, Norway.*
E-mail: kim.s.mews@gmail.com
[2] *SINTEF, Formation Physics,* 7031 *Trondheim, Norway*
[3] *National Cooperative for the Disposal of Radioactive Waste,* 5430 *Wettingen, Switzerland*

Accepted 2023 December 28. Received 2023 December 15; in original form 2023 April 3

SUMMARY

We conducted an extensive study on the elastic properties of Opalinus Clay and the overlying and underlying rock formations, which range in the overall clay mineral content from nearly 0 to 60 wt.%. Our laboratory experiments focused on seismic and ultrasonic frequencies to determine the extent to which seismic dispersion affects elastic parameters and seismic wave velocities. The results comprise the static stiffness from undrained triaxial cycles (axial–confining stress: 8–10 MPa), the dynamic stiffness at seismic frequencies (0.5–143 Hz), intrinsic attenuation (0.5–20 Hz), compressional velocity measurements (0.5–2 Hz) and ultrasonic velocity measurements (250 and 500 kHz). We compared these laboratory results to in situ sonic logging measurements to assess the role of frequency in measured elastic parameters. The results suggest a notable correlation between clay mineral content and dispersion. Specifically, high clay mineral content leads to increased dispersion, even within the seismic frequency band. The overall dispersion of *P*-wave velocity in the frequency range from 1 Hz to 500 kHz is up to 16%. This frequency dependency is crucial when establishing a relationship between sonic well log data and static stiffness for geomechanical modelling. The results are discussed with respect to possible dispersion mechanisms, including the role of bound water in clay.

Key words: Elasticity and anelasticity; Microstructure; Geomechanics; Acoustic properties; Seismic attenuation; Wave propagation.

1 INTRODUCTION

Elastic wave velocities in rocks can be dispersive between seismic, sonic and ultrasonic frequencies, which will impact the inferred dynamic moduli. Elastic velocities in laboratory studies are usually measured at ultrasonic frequencies (10^5–10^6 Hz). Under in situ conditions in the borehole, however, acoustic velocities are measured in the kHz region. Studies have shown a significant difference between velocities from sonic logs, and ultrasonic velocity measurements in the laboratory (Murphy 1982; Moos & Zoback 1983; Goldberg & Zinszner 1989). An important source for these differences are macrocracks, but the composition and microcracks significantly affect the velocities, too (Moos & Zoback 1983). The variation between sonic logs and ultrasonic velocity measurements becomes even larger due to the ultrasonic wavelength being much smaller than heterogeneities, which leads to scattering effects (Marion & Coudin 1992). Additionally, a different scale of the two measurement techniques contributes to different results.

Even for dynamic properties from laboratory measurements, a frequency dependence in elastic parameters and wave velocities is observed (Jones 1986; Murphy *et al.* 1986; Tutuncu *et al.* 1998; Chapman 2003; Holt *et al.* 2016; Rivière *et al.* 2016; Lozovyi *et al.* 2018; Szewczyk *et al.* 2018a; Lozovyi & Bauer 2019b; Alkhimenkov *et al.* 2020; Rørheim *et al.* 2022). The dispersion is not only significant for higher frequencies but also in the seismic frequency band (Spencer 1981; Batzle *et al.* 2006; Tisato & Madonna 2012; Mikhaltsevitch & Lebedev 2014; Pimienta *et al.* 2015b; Szewczyk *et al.* 2016). Often times low-frequency dispersion in fully saturated samples can be explained by the transition from drained to undrained conditions Pimienta *et al.* (2015a). An extensive summary is provided by Rørheim (2022). Especially clay-rich materials appear to exhibit strong frequency dependence (Suarez-Rivera *et al.* 2001; Duranti *et al.* 2005; Szewczyk *et al.* 2018b; Mikhaltsevitch *et al.* 2021b, a). Lozovyi & Bauer (2018) show that Opalinus Clay from the Mont Terri Rock Laboratory exhibits a strong frequency dependence: The dynamic Young's modulus might change by a factor of 2 when comparing seismic to ultrasonic frequencies.

Dispersion in shale is not yet fully understood. There are several possible mechanisms (see Mavko *et al.* 2009; for an overview), and

probably more than one of them contributes to dispersion between seismic and ultrasonic frequencies. Shales are characterized by permeabilities in the nanoDarcy range, up to μDarcy for sandy shales. This eliminates global (Biot) flow as a dispersion mechanism since the transition frequency between low and high-frequency behaviour is likely to be well above ultrasonic frequencies commonly applied in the laboratory.

Dispersion in sedimentary rocks is often described by squirt flow between soft and stiff pores, where soft pores may incorporate microcracks. For water-saturated soft pores or cracks with an aspect ratio of 0.001, the transition frequency between low and high-frequency behaviour would typically be in the kHz regime, that is close to logging frequencies but well below ultrasonic frequencies. The transition frequency increases with the aspect ratio raised to a power of 3 (Mavko *et al.* 2009) and is inversely proportional to pore fluid viscosity. Lower aspect ratio cracks, which would lead to squirt dispersion in the low-frequency range, tend to be closed under applied effective stresses of 10 MPa or more (Mavko & Nur 1978). Thus, the traditional squirt flow mechanism does not explain our observation of low-frequency dispersion. Clay-squirt represents a possible dispersion mechanism in the ultrasonic range for shaly sandstones (Marketos & Best 2010; Sørensen & Fabricius 2017).It applies when a compression wave travels through a shaly sandstone, where it could squeeze the softer clay part, creating local pressure differences, which might cause the fluids in the micropores of the clay to be pushed out into the larger pores of the rock (Best & McCann 1995). With permeabilities as low as nanoDarcy–microDarcy, the transition frequency is, however, likely to be well above the ultrasonic frequencies applied here.

Hence, this mechanism cannot explain dispersion within the seismic frequency range. Saturation (or permeability) heterogeneities lead to so-called patchy saturation. The transition frequency is proportional to permeability and inversely proportional to viscosity and to the square of patch size. For nanoDarcy–microDarcy shales and patches on the millimeter scale, transition frequencies will range from sub-Hz to the seismic range. Water inside clay minerals and on solid mineral surfaces will, however, have very different properties from free water: Zhu & Granick (2001) measured viscosities of 10^5–10^7 Pa·s in an aqueous solution with 25 mM salt content at a distance corresponding to 1–2 monolayers of water from a mica surface. Laboratory experiments (Antognozzi *et al.* 2001; Zhu & Granick 2001) indicate that water within the first nanometer may have non-zero shear modulus and viscosity 10^4–10^9 times larger than of free water. This may contribute to P- and S-wave velocities, particularly at higher frequencies. Such bound water can be considered as a viscoelastic substance that will have an impact on the mechanical behaviour of clays and shales with large specific surfaces and may be modelled accordingly (Holt & Fjær 2003; Holt & Kolstø 2017). Bound water may also be considered with the other dispersion models discussed above: Squirt flow of bound water could take place at seismic frequencies. This will be further addressed in the discussion section.

Overall, we see a frequency-dependent elasticity, whereas dynamic moduli are larger than static. The rocks become stiffer with increasing frequency, indicated by Young's modulus E: $E_{\text{ultrasonic}} > E_{\log} > E_{\text{low-frequency}} > E_{\text{static}}$ (Tutuncu *et al.* 1998). The lowest stiffness is expected for static properties due to dispersion and non-elastic effects (Lozovyi & Bauer 2018). But strain rate, strain amplitude, drainage conditions, heterogeneities and anisotropy have a significant effect, too (Fjær 2019).

Opalinus Clay is the designated host rock for radioactive waste disposal in Switzerland, and it has comparable properties to many caprocks for natural geological reservoirs. The sites currently investigated for a deep geological repository are located some 50–100 km to the east of the Mont Terri Rock Laboratory, where Opalinus Clay is encountered at greater depths and in a much less deformed area. Geomechanical characterization of Opalinus Clay and confining units is important for engineering design (access and underground structures) and assessment of long-term safety. Therefore, we tested preserved core plugs of different rock formations from boreholes and analysed the role of frequency in measured elastic parameters and wave velocities. We performed quasi-static loading–unloading cycles, low-frequency measurements from 0.5 to 143 Hz, low-frequency measurements from 0.5 to 2 Hz at uniaxial strain and ultrasonic velocity measurements and compared the laboratory results to well-logging data obtained from two boreholes. The objective is to evaluate the frequency dependence. We clarify which mechanisms should be accounted for in geomechanical modelling when sonic logging data is used to obtain static parameters and discuss the results with respect to possible dispersion and attenuation mechanisms, including the role of bound water in clay minerals.

The role of clay mineral content is of particular interest as it is known to exert a strong influence on hydromechanical properties in clastic-sedimentary sequences (Bourg 2015). It has a profound effect on the microstructure, as manifested in pore size and high reactive surface area (e.g. retention properties), which in turn controls both hydraulic and mechanical properties. Furthermore, clay content can satisfactorily be estimated quantitatively (e.g. using geophysical logging in combination with XRD measurements as outlined in the paper). This means that from an extensive geophysical logging and laboratory testing program, continuous data is 'available' for both dynamic elastic properties (sonic scanner and density) as well as clay mineral content. To the best of our knowledge, there are no existing studies comparing samples with varying clay content (nearly 0–60 wt.%) from seismic to ultrasonic frequencies.

2 MATERIALS AND METHOD

2.1 Sample characterization

We tested nine samples from five different formations. The rocks were drilled from preserved cores from boreholes Trüllikon-1-1 (TRU-1) and Bülach-1-1 (BUL1-1) that were drilled within Stage 3 of the Sectoral Plan for Deep Geological Repositories for radioactive waste in Switzerland (Fig. 1). The target formation is the Opalinus Clay with a thickness of 104 m in BUL1-1 (Jordan *et al.* 2021) and 112 m in TRU1-1 (Schwarz *et al.* 2021). We tested samples from different subfacies within the Opalinus Clay and from over- and underlying formations. The samples vary in clay mineral content and cover a broad spectrum from nearly 0 wt.% to more than 60 wt.% (Fig. 2). A detailed clay mineralogy for the formations of the samples with the highest clay mineral content is shown in Fig. 3.

Opalinus Clay was extensively characterized at the Mont Terri Rock Laboratory in western Switzerland, at approximately 220–320 m of overburden (Bossart *et al.* 2017). The studies by Lozovyi & Bauer (2018) and Lozovyi *et al.* (2018) in a triaxial setup included low-frequency measurements. Here, the study is extended to characterize Opalinus Clay from deep boreholes at depths of 850–920 m. An overview of the well logging information (Gonus *et al.* 2021) is shown in Fig. 4.

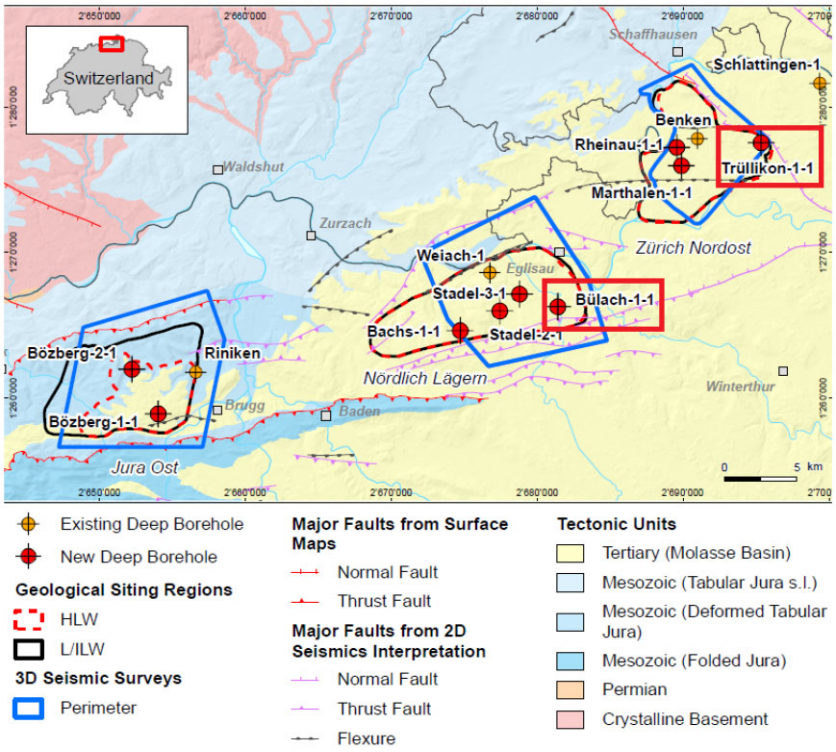

Figure 1. Geological map of the locations of the boreholes TRU1-1 and BUL1-1. Both boreholes are located in the North of Switzerland close to the German border (red rectangle, map top left and red rectangle around the borehole location).

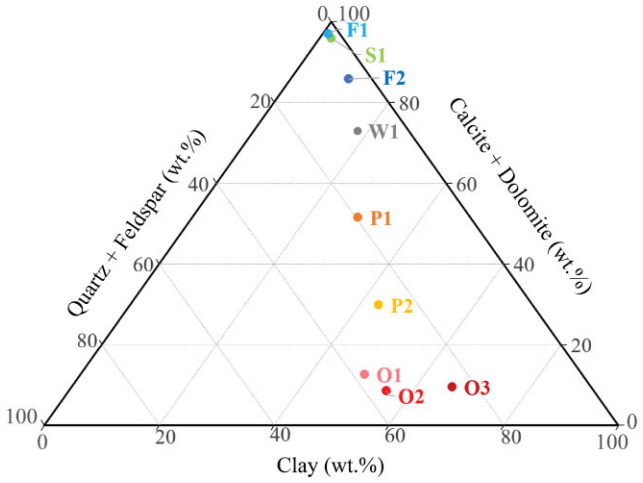

Figure 2. Ternary diagram indicating the mineral content in wt.%. The bottom left corner represents 100 wt.% quartz and feldspar, the top centre 100 wt.% carbonates (calcite and dolomite) and the bottom right 100 wt.% clay minerals. The abbreviations of the formations are further explained in Table 1. The core sample O3 has the highest clay content, whereas F1 contains almost no clay minerals.

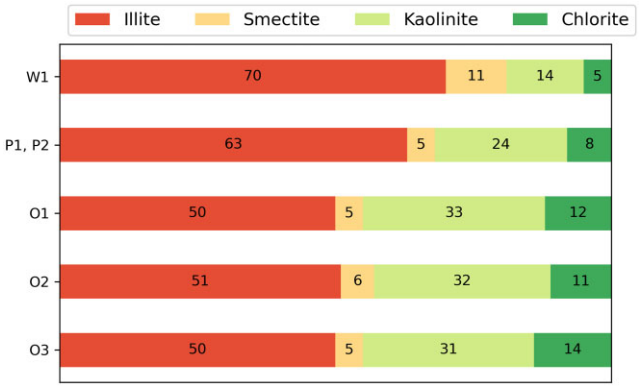

Figure 3. The percentage distribution of the clay mineral content end-members was derived in two steps: (i) the relative amount of clay types was determined by Full-Pattern-Fit (FPF) method (Dumon & Van Ranst 2016), (ii) the individual clay types and groups are calculated from 35 clay structures relevant for clays in sedimentary rocks in Switzerland. The FPF method fits the measured XRD patterns to a set of predefined patterns by the least square procedure.

The samples are considered fully water-saturated under the respective in situ conditions, based on laboratory tests (water-loss and He pycnometry). We determined the bulk density ρ_b, water content w and porosity ϕ from desiccation at 105 °C. The mineralogical composition has been provided from X-ray diffraction (XRD) analysis. An overview of the geological and mineralogical description of the samples is shown in Table 1.

2.2 Sample preparation

Based on X-ray computed tomography (CT) scans and core photographs, we identified zones with visible cracks and prominent inhomogeneities that we avoided for sample selection. We drilled and trimmed the core plugs normal to the bedding plane with a diameter of 25.4 mm and a length of 48–52 mm. Afterwards, the samples were stored in Marcol oil to maintain the in situ water content. During the loading procedure, the samples were exposed to brine with a composition as indicated in Table 2.

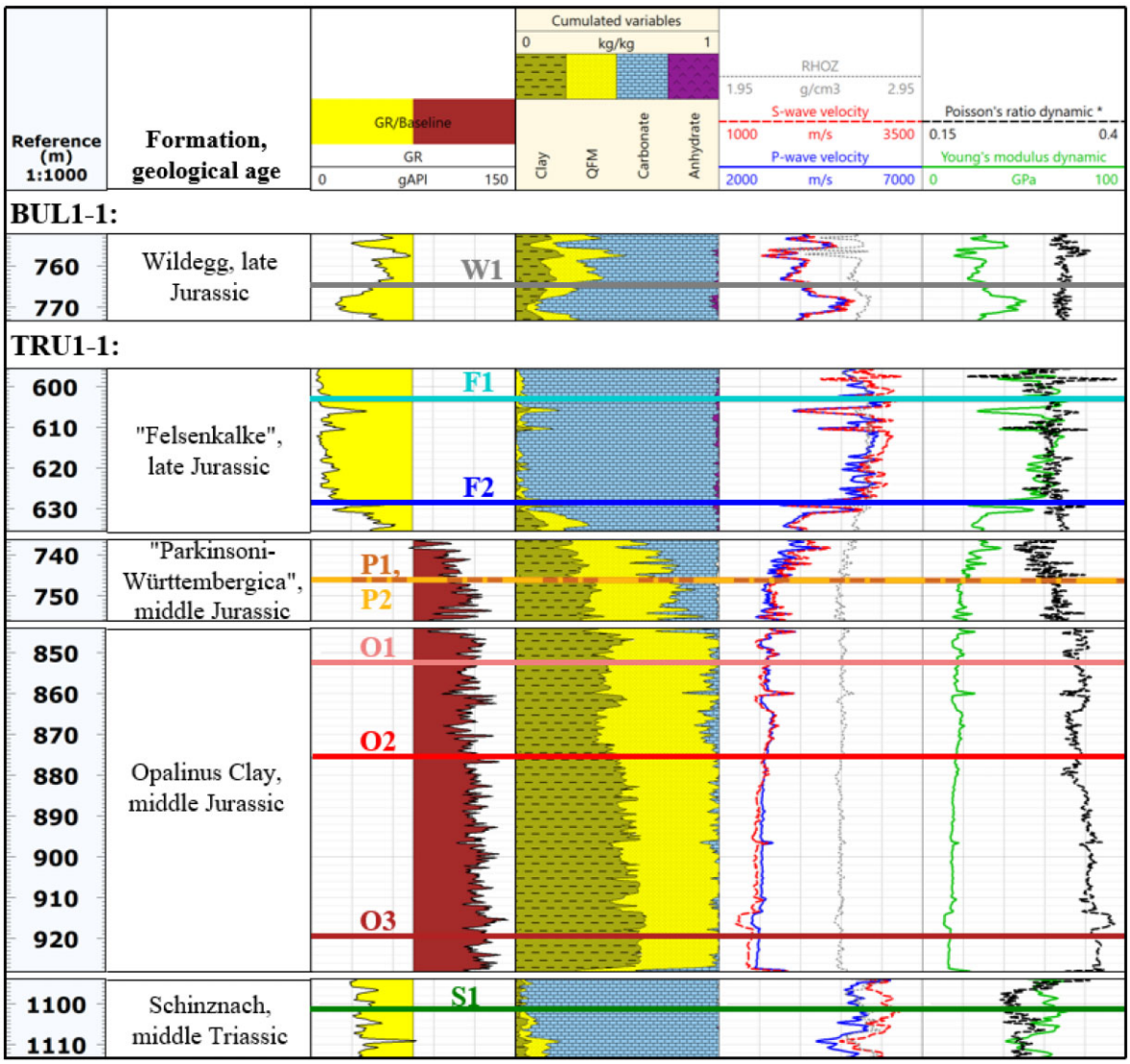

Figure 4. Well logging information for the five different formations (see Table 1). Horizontal coloured lines indicate the depth of the respective core samples. *GR* indicates Gamma Ray count in gAPI with a baseline at 75, indicating samples with lower clay content to the left and samples with increased clay content to the right. Further, *Cumulated variables* show the mineral content computed from mineral inversion for clay, QFM (quartz, feldspar, mica), carbonate and anhydrate and *RHOZ* the bulk density. *P*-wave and *S*-wave velocities were calculated from DTCO (*P*-wave), and DTSM (*S*-wave) measurements. Poisson's ratio and Young's modulus were computed using Hooke's law. Sonic logging data were sampled every 15 cm.

2.3 Experimental setup

The experiments were performed in the low-frequency cell at the Formation Physics laboratory at SINTEF (Fig. 5). It is essentially a triaxial pressure cell with independent control of axial and radial stress as well as pore pressure (Szewczyk *et al.* 2016). We wrapped a mesh around the sample for side drainage, allowing for faster pore pressure equilibrium. Similar low-frequency measurements have been performed in different laboratories (Batzle *et al.* 2006; Tisato & Madonna 2012; Mikhaltsevitch & Lebedev 2014; Pimienta *et al.* 2015b; Spencer & Shine 2016).

Table 3 gives an overview of the four different measurement techniques and their terminology. It is important to note that these measurements were performed through very different techniques. Ultrasonic velocity measurements record the traveltime of a transmitted *P*- and *S*-wave. Whereas dynamic stiffness measurements at seismic frequencies measure the stress–strain response using the forced oscillation concept (Spencer 1981). Direct *P*-wave modulus measurements are performed in the same way as dynamic stiffness measurements at seismic frequencies but under uniaxial strain conditions. The static stiffness is determined by triaxial stress-strain measurements. The different techniques and the resulting uncertainties in comparing these techniques are discussed below.

2.3.1 *Ultrasonic velocity*

The ultrasonic velocity measurement is performed by standard pulse-transmission technique (Hughes *et al.* 1949) with strain amplitudes between 10^{-7} and 10^{-6}, measuring the resulting *P*- and *S*-wave velocities in the axial direction. The ultrasonic *P*- and *S*-wave transducers have a central frequency of 500 and 250 kHz, respectively, mounted inside titanium end-caps. The error of the ultrasonic *P*-wave measurements is expected to be less than 1% (Lozovyi & Bauer 2019a). The error for the *S*-wave might be higher as it may be superposed with a strong, converted *P*-wave signal.

Table 1. The tested formations with sample ID show the geological properties and the mineralogy. The abbreviation n/a stands for *no answer*, indicating too low concentrations to be captured or the absence of a mineral. The letters *tr* stand for trace, indicating very small amounts of the respective mineral. The abbreviation *w* stands for water content, ϕ for porosity, *S* for sulphur and *C* for carbon.

Sample ID	W1	F1	F2	P1	P2	O1	O2	O3	S1
Formation	Wildegg	'Felsen-kalke'	'Felsen-kalke'	'Parkin-soni-Württem-bergica'	'Parkin-soni-Württem-bergica'	Opalinus Clay	Opalinus Clay	Opalinus Clay	Schinznach
Geological-Description	Argillaceous limestone	Lime-stone	Lime-stone	Calcareous marl	Sandy/silty marl	Sandy/silty claystone	Sandy/silty claystone	Clay-stone	Dolo-stone
Sample depth [m]	764.71	603.66	628.72	746.28	746.55	852.05	875.77	919.31	1101.10
Bulk density [g/cm]	2.64	2.68	2.66	2.59	2.53	2.55	2.54	2.55	2.61
w [%]	1.9	0.7	1.8	4.2	3.4	3.6	4.3	4.7	5.6
ϕ [%]	4.9	1.8	4.7	10.6	8.8	9.1	10.5	11.6	13.8
Minerals [wt.%]									
Quartz	6	2	3	14	22	27	25	15	2
K-feldspar	3	tr	1	4	3	6	6	5	tr
Plagioclase	tr	tr	<1	1	1	3	3	3	tr
Calcite	73	89	82	47	26	12	8	9	0
Dolomite	0	8	3	3	3	0	0	0	96
Siderite	tr	tr	n/a	n/a	n/a	4	4	3	0
Pyrite	0.2	0	<0.1	<0.1	0.8	0.5	0.4	0.5	0
Clay	18	1	10	28	42	47	52	63	2
C (org)	0.41	0.16	0.35	1.01	0.9	0.91	1.07	1.03	0.68
S	0.13	<0.05	<0.05	<0.05	0.44	0.28	0.2	0.28	<0.05
C (inorg)	8.77	11.69	10.24	6.11	3.5	1.79	1.37	1.47	12.45

Table 2. Brine composition for application of pore pressure to the preserved core samples under testing.

Compound	g $(kg_{H_2O})^{-1}$	mmol $(kg_{H_2O})^{-1}$
NaCl	6.736	115.3
Na_2SO_4	3.409	24.0
$MgCl_26H_2O$	1.864	9.2
$CaCl_22H_2O$	1.751	11.9
KCl	0.190	2.6
$NaHCO_3$	0.046	0.5

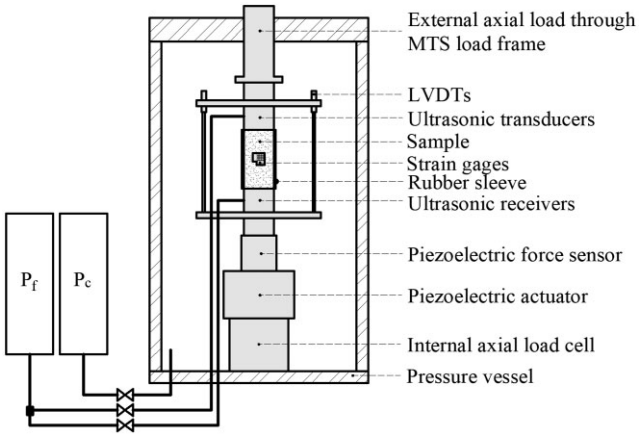

Figure 5. Schematic drawing of the low-frequency cell at SINTEF. The confining pressure P_c and the pore pressure P_f are regulated by external pumps. A detailed explanation of the experimental setup can be found in Szewczyk *et al.* (2016) and for the direct *P*-wave modulus measurement setup in Lozovyi & Bauer (2019b).

The ultrasonic *P*- and *S*-wave phase velocities are calculated in axial direction using the following equation:

$$V_{P,S} = \frac{L}{t - t_0}, \tag{1}$$

where L is the sample length, t is the sample traveltime and t_0 is the system traveltime. The procedure of arrival picking from previous studies (Szewczyk *et al.* 2018b) has been used. We calibrated the system before and after the test with an aluminium standard sample and pick as arrival the first maximum as shown in Fig. 6(a) for the *P*-wave and in Fig. 6(b) for the *S*-wave.

2.3.2 *Dynamic stiffness at seismic frequencies*

To determine the dynamic stiffness at seismic frequencies, a different measurement technique is required since the wavelength of a seismic wave is much longer than the sample dimension. Therefore, Young's modulus and Poisson's ratio are calculated from stresses and strains. The measurements are performed at 13 frequencies ranging from 0.5 to 143 Hz under axial deviatoric stress of 0.5 MPa. The sample is excited by a piezoelectric displacement actuator at a given frequency, resulting in force modulation measured by a piezoelectric force sensor. Strain modulations were measured by eight strain gauges (four axial, four radial) attached to the sample's surface. The strain gauges are connected to four Wheatstone bridges with the half-bridge configuration: strains on the opposite sides of the sample are averaged by the bridge. These measurements were performed under uniaxial stress conditions, where we adjusted the axial strain modulations to 10^{-6} to stay within the elastic regime (Winkler *et al.* 1979). Lozovyi & Bauer (2019b) provide error analysis of the low-frequency measurements. The systematic error for Young's modulus ranges from −4 to −1.2%, while for Poisson's ratio, the absolute error ranges from −0.016 to −0.008. The random error within a single test for Young's modulus is ±0.7%, while for Poisson's ratio, it is ±0.008. The dynamic stress magnitude is calculated from the force amplitude F and the cross-sectional area of the sample A as follows:

$$\sigma_{ax} = \frac{F_{ax}}{A}. \tag{2}$$

The dynamic strain amplitudes ε_{ax} and ε_r are calculated as follows:

$$\varepsilon_{ax} = \frac{2B_{ax}}{V_{ax}G_F}; \varepsilon_r = \frac{2B_r}{V_{ax}G_F}, \tag{3}$$

whereas B_{ax} and B_r are the voltage amplitudes from axial and radial Wheatstone Bridges containing strain gauges attached to the sample, respectively, V_{ax} is the bridge excitation voltage and G_F is the gauge factor. Young's modulus and Poisson's ratio are then calculated from the ratio of σ_{ax} to ε_{ax} and the negative ratio of ε_r to ε_{ax}, respectively.

2.3.3 *Direct P-wave modulus*

Another set of low-frequency measurements was performed under uniaxial strain conditions, called direct *P*-wave modulus measurements. This technique synchronizes the axial force and confining pressure modulations to obtain *P*-wave modulus C_{33} at seismic frequencies at uniaxial-strain ($\varepsilon_r = 0$) conditions. Uniaxial-strain conditions are achieved by radial stress oscillations inside the pressure vessel and are calculated as follows (Lozovyi & Bauer 2019a):

$$C^e_{33} = \frac{\sigma_{ax}}{\varepsilon_{ax}} \tag{4}$$

$$V_P = \sqrt{\frac{C_{33}}{\rho_b}}. \tag{5}$$

This technique allows for a direct comparison of seismic and ultrasonic stiffness measurements. The advantage of this study is that it allows for direct estimation of axial *P*-wave velocity normal to bedding in anisotropic samples using only one core plug. The technique reduces the error in *P*-wave modulus caused by inverting several elastic parameters from differently oriented core plugs from up to 20% to only up to 6%. The systematic error in low-frequency *P*-wave velocity is up to −3%.

Attenuation was obtained from phase angle δ between the applied stress and the resulting axial strain (Jackson *et al.* 1984):

$$1/Q = \tan\ \delta. \tag{6}$$

We measured attenuation for Young's modulus from 0.5 to 20 Hz and for the *P*-wave modulus from 0.5 to 2 Hz.

2.3.4 *Static stiffness*

During the entire test, it is possible to derive the quasi-static isostress bulk axial deformation with measurements from three LVDTs. The static stiffness E_{stat} is derived as follows:

$$E_{stat} = \frac{\Delta\sigma_{ax}}{\Delta\varepsilon_{ax}}. \tag{7}$$

We further apply the model by Fjær *et al.* (2013) in order to quantify non-elastic effects and to find the 'true' elastic modulus, which is comparable to the dynamic modulus at low frequency with

Table 3. Overview of acquired data and its terminology from high to low frequencies in descending order. All tests were executed under undrained conditions.

	Measurement	Terminology
1	ultrasonic velocity (250–500 kHz)	Ultrasonic velocity
2	LF (0.5–143 Hz)	Dynamic stiffness at seismic frequencies
3	LF (0.5–2 Hz) at uniaxial strain	Direct *P*-wave modulus
4	Quasi-static loading-unloading cycles	Static stiffness

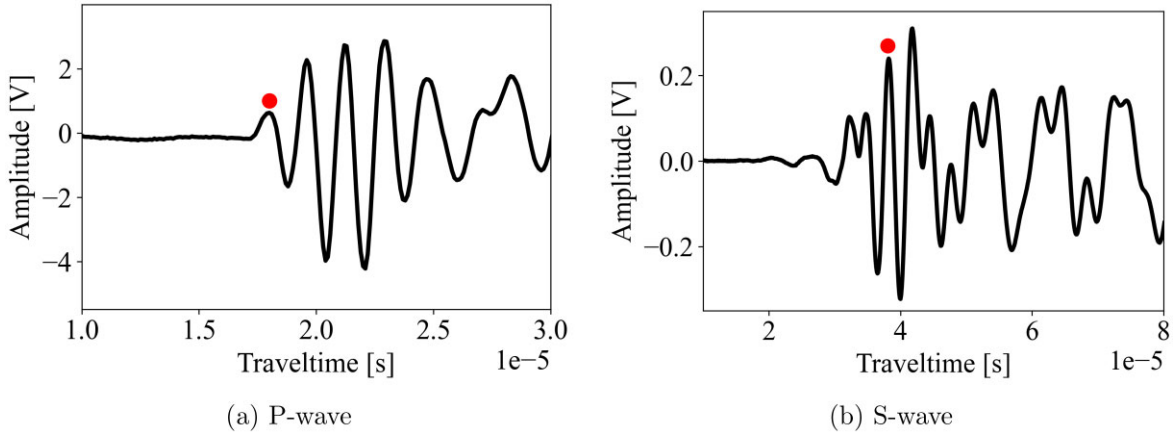

Figure 6. Signature waveform at a central frequency of 500 kHz for sample F1: the red circle indicates the first maximum of the *P*- and *S*-wave arrival, respectively.

an equivalent strain rate. The difference between static and dynamic moduli is defined as non-elastic compliance, which increases linearly with stress change independent of mineralogy (Fjær *et al.* 2011, 2012, 2013; Lozovyi *et al.* 2017). Fjær *et al.* (2013) express non-elastic compliance during unloading S as follows:

$$S = \frac{1}{C_{33}} - \frac{1}{C_{33}^3} = a\left(\sigma_{ax}^0 - \sigma_{ax}\right) + b, \tag{8}$$

whereas a and b are constants and σ_{ax}^0 is the stress at the beginning of the unloading path. Fig. 7(a) shows an example of a stress/strain curve for sample P2. The red circle indicates σ_{ax}^0, where $S = b$.

Similarly, Lozovyi *et al.* (2017) quantify the dependence of rock stiffness on the stress change through a semi-empirical model assuming a linear relationship between the incremental compliances $\mathrm{d}\varepsilon_{ax}/\mathrm{d}\sigma_{ax}$ and $\mathrm{d}\varepsilon_{\mathrm{rad}}/\mathrm{d}\sigma_{ax}$ and the axial stress change. To calculate the stiffness parameters based on stress amplitude, we first find the average strains and integrate these values. This process provides us with the average compliance in the direction along the axis, as described in Lozovyi *et al.* (2017):

$$\frac{\Delta\varepsilon_{ax}}{\mathrm{d}\sigma_{ax}} = \frac{a_{ax}\cdot\Delta\sigma_{ax}}{2} + \left(\frac{\mathrm{d}\varepsilon_{ax}}{\mathrm{d}\sigma_{ax}}\right)_0, \tag{9}$$

and in the radial direction:

$$\frac{\Delta\varepsilon_{r}}{\mathrm{d}\sigma_{ax}} = \frac{a_{r}\cdot\Delta\sigma_{ax}}{2} + \left(\frac{\mathrm{d}\varepsilon_{r}}{\mathrm{d}\sigma_{ax}}\right)_0, \tag{10}$$

where the constant a_{ax} (axial non-elasticity parameter) and a_r (radial non-elasticity parameter) define the linear increase of compliance with stress $\Delta\sigma_{ax}$, respectively, at $\Delta\sigma_{ax} = 0$ at the beginning of unloading, where the stiffness is maximal. Fig. 7(b) shows the graphical solution, whereas the red point indicates the zero-stress extrapolated compliance. The zero-stress Poisson's ratio is given by:

$$\nu_0 = -\left(\frac{\mathrm{d}\varepsilon_{r}}{\mathrm{d}\sigma_{ax}}\right)_0 \Big/ \left(\frac{\mathrm{d}\varepsilon_{ax}}{\mathrm{d}\sigma_{ax}}\right)_0. \tag{11}$$

2.3.5 Resulting uncertainties from comparing different measurement techniques

Possible errors of low-frequency measurements are extensively discussed in Lozovyi & Bauer (2019a) and emphasized below concerning the direct relationship between dynamic stiffness, material density and its velocity.

The heterogeneity of the sample plays a decisive role as strains are measured on an area of 10 mm^2 and the surrounding strain field, whereas stress is measured over the entire sample. It is important to note that we selected the sample from a homogeneous part, assuming the stiffness measured on a small sample is representative of the material stiffness on the wavelength scale for direct comparison to ultrasonic velocity.

An error in rock density may cause further uncertainties. It is obtained from the sample length, diameter and weight of the sample prior to the start of the test. Testing at elevated confining stress can change the sample dimension and the sample material, especially for shale, which might swell under full saturation, which changes the sample dimensions. Ultrasonic measurements are corrected for the change in length, the deformation of the piston, confining pressure and axial stress. So this error may only lead to uncertainties for dynamic measurements at seismic frequencies. This error has been calculated and can be neglected Lozovyi & Bauer (2019a). For the triaxial cycle, LVDT measurements are corrected for changes in confining and axial stress and can be directly compared to ultrasonic measurements. For all tests, measurement results from LVDTs and strain gauges are in agreement. This indicates that we can directly compare dynamic stiffness measurements at seismic frequencies to ultrasonic velocity measurements.

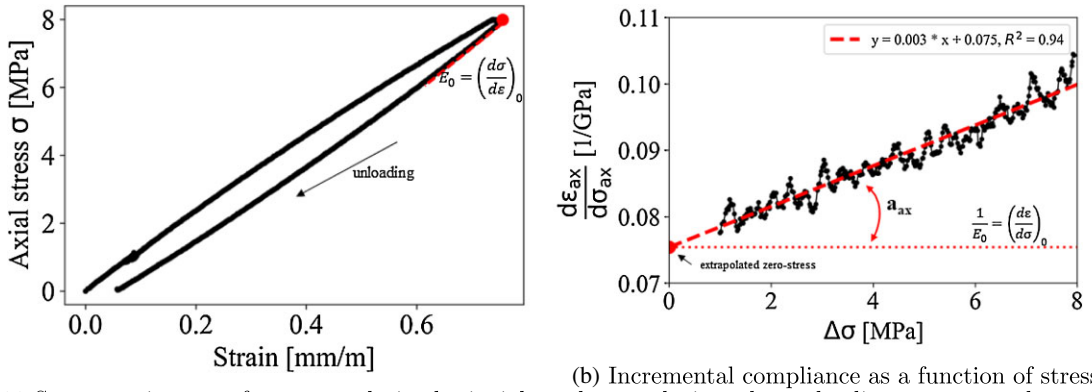

(a) Stress-strain curve from an undrained triaxial loading/unloading cycle with 8 MPa stress amplitude: the red point indicates the onset of the unloading, with the highest stiffness.

(b) Incremental compliance as a function of stress change during the unloading segment: the red point indicates the compliance extrapolated to zero stress change, which indicates the pure elastic response of the rock.

Figure 7. Example of sample P2 to indicate how inelastic effects in static stiffness were obtained.

2.4 Test protocol

The test protocol applied to each sample can be subdivided into four major steps and is shown as an example for sample P1 in Fig. 8:

(i) *Initial loading and pore fluid exposure*:
The confining pressure was increased to 10 MPa at a rate of approximately 4 MPa/ hr. At about 8 MPa, the sample was exposed to synthetic pore fluid (see Table 2) at a pore fluid pressure of $p_f = 1$–1.5 MPa against a backpressure valve. Yurikov *et al.* (2019) found that the dominating factors and resulting dependencies of elastic moduli during hydration for Opalinus Clay are the change in total porosity and pore-filling fluid, stiffness change in contacts between clay particles, and chemical softening of clay particles. To minimize these effects, the loading continues during pore fluid exposure to compensate for sample swelling. The confining pressure p_c and the pore fluid pressure were subsequently simultaneously increased to 15 and 5 MPa, respectively.

(ii) *Consolidation and Skempton B measurement*: After the sample's consolidation, we closed the outlet valve and performed an undrained hydrostatic loading-unloading cycle (Skempton B) with a stress amplitude of 1 MPa. These values were not corrected for compliance (Ghabezloo & Sulem 2010).

(iii) *Low-frequency measurement*: The sample is stable at p_c of 15 MPa, axial deviatoric stress σ_{ax} of 1 MPa and p_f of 5 MPa, resulting in an effective stress p_c' of 10 MPa. Tests were performed at effective stresses of 10 MPa to achieve in situ conditions in the concerned depth range, which range from approximately 8 MPa for sample F1 (shallowest, 603 m depth) and 13 MPa for sample S1 (deepest, 1101 m depth). To exclude potential effects of variable stress conditions, all laboratory tests were done at the same effective confining stress, which was chosen at 10 MPa.

(iv) *Undrained static triaxial measurement*: We increased the axial stress for the loading cycle between 8 and 10 MPa. Once it reached the maximum load, we decreased the axial stress immediately. The stress cycle amplitudes were 8 MPa for the samples W1, P1, P2 and O3, and 10 MPa for the samples F1, F2, O1, O2 and S1.

The following parameters are measured and recorded as a function of time: axial stress, radial stress, pore pressure, axial strain from LVDTs and strain gauges, radial deformation from strain gauges, and temperature (inside and outside of the cell). Compressional and shear-wave ultrasonic velocities were recorded throughout the entire test but evaluated and averaged after the Skempton *B* cycle and before applying axial stress. All tests were performed at room temperature.

3 RESULTS

An overview of the data is summarized in Table A1.

3.1 Skempton B

The measured values of Skempton's *B* (Table 4) are representative of water-saturated rocks. Unfortunately, no direct measurement of Biot's α was made as part of our campaign. We can estimate α from poroelasticity theory, using measured undrained bulk modulus and *B* as input, but then we need to assume values for the effective solid grain modulus. This can be done based on mineralogy, but clay moduli are not straightforward to implement since they have to account for immobile (bound) water. Using values from 35 to 40 GPa for the samples with the smallest clay content down to 10–15 GPa for the samples having the highest clay content, we find Biot coefficients between 0.5 and 1, keeping the pore fluid bulk modulus 2.4 GPa (which is the value from Batzle & Wang (1992) for 3.5% salinity brine at room temperature and 5 MPa fluid pressure). Assuming a value significantly lower, such as less than 1 GPa, leads to estimated Biot coefficient values that surpass 1 and veer into unrealistic territory. It is, however, possible in the case of patchy saturation that the effective water bulk modulus could be somewhat reduced, still leading to realistic values for α.

3.2 Dynamic stiffness—seismic frequencies

The results of the low-frequency measurements for Young's modulus are shown in Figs 9(a) and (b). Fig. 9(a) shows that Young's modulus for tested samples ranges from 12 to 75 GPa. Fig. 9(b) demonstrates seismic dispersion of Young's modulus on a normalized *y*-axis. It indicates that samples with a lower clay content exhibit no dispersion, whereas samples with a high clay content show significant dispersion in the seismic frequency band of up to 13%. Shale usually exhibits large dispersion, even within the seismic frequency band. Szewczyk *et al.* (2018a) measured seismic dispersion of 11% for Mancos shale at a relative humidity of 100%, Lozovyi & Bauer (2018) found seismic dispersion to be larger than 10% for

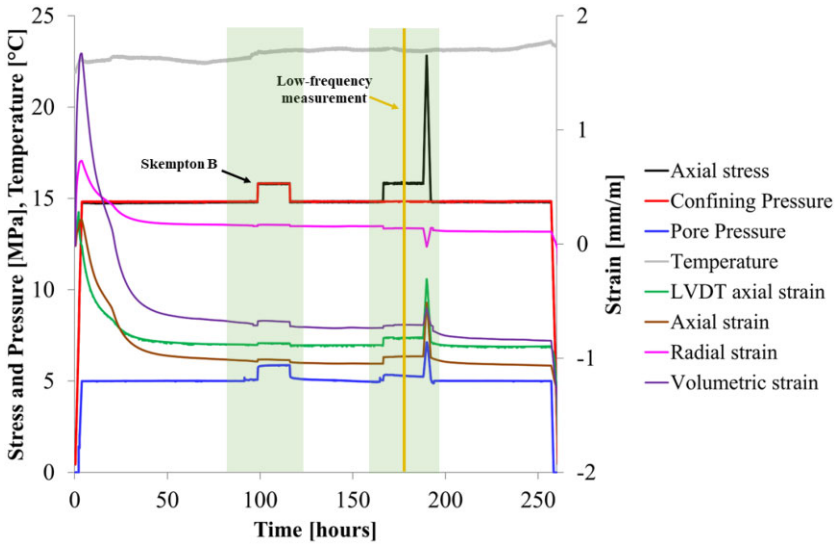

Figure 8. Testing Protocol for Sample P1 illustrating the confining pressure, axial stress and pore pressure conditions (drained/undrained) during the testing period. The vertical orange line marks the conditions during the low-frequency measurement. Notably, the pore pressure remained undrained during the Skempton B, low-frequency, and static triaxial measurements marked as green rectangles in the plot. Compressive strains are depicted as positive, while extensive strains are negative.

Table 4. Measured Skempton *B* coefficients.

Sample ID	W1	F1	F2	P1	P2	O1	O2	O3	S1
Skempton B coefficient	0.86	0.84	0.6	0.8	0.74	0.81	0.82	0.82	0.75

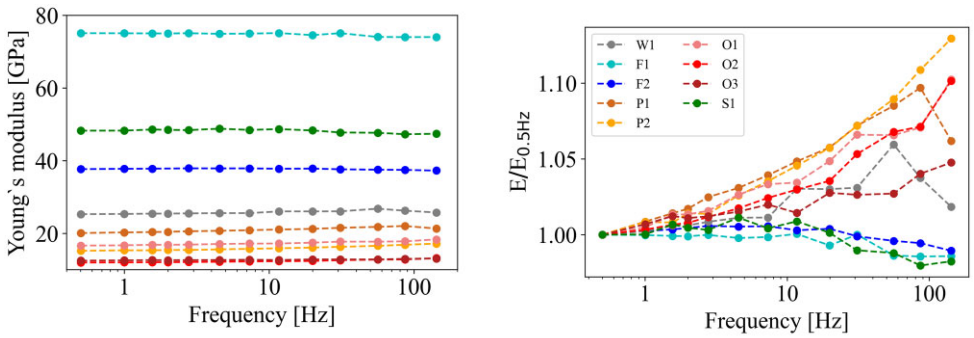

(a) Young's modulus (b) Normalized Young's modulus

Figure 9. Low-frequency measurement results: vertical Young's modulus as a function of frequency for the nine different tested samples, respectively.

Opalinus clay, for both sandy and shaly facies and Lozovyi & Bauer (2019b) measured seismic dispersion of even 16% for Opalinus clay. On the other hand, seismic dispersion for sandstones is much lower. Chapman *et al.* (2017) show seismic dispersion of about 7% for 100% saturated Berea sandstone.

Fig. 10 shows Poisson's ratio versus frequency. Overall, it varies from 0.26 (sample O3 and S1) to 0.34 (sample O1) without a clear trend. Lozovyi & Bauer (2018) did not observe a trend for Poisson's ratio for measurements on Opalinus clay either.

3.3 Dynamic stiffness—multifrequency comparison

For this study, the main motivation was to achieve an overall comparison between laboratory data at seismic and ultrasonic frequencies and sonic logging data from the wellbore. To get both field and laboratory data spanning a wide frequency range to demonstrate the frequency dependence of *P*-wave velocities is rather rare due to

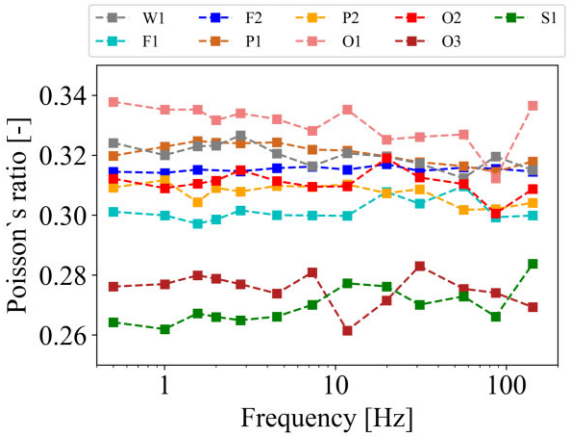

Figure 10. Poisson's ratio as a function of frequency.

the complexity of these measurements. We performed tests to show the overall *P*-wave dispersion from 1 Hz to 250 kHz (Fig. 11). The results imply that the *P*-wave dispersion varies from 3% (sample F1) to 16% (sample O2) with an average of 11%. *S*-wave velocities show a similar trend, with sonic logging velocities being lower than ultrasonic velocities except for sample S1 (Fig. 12).

The velocities obtained from sonic well logs tend to be lower than those measured at ultrasonic frequency in the laboratory. The estimated range for the sonic *P*-wave velocity is 85–100% of the ultrasonic velocity, with a most likely value of 93%. For the sonic *S*-wave velocity, the estimated range is 86–105% of the ultrasonic velocity, with a most likely value of 95%.

Low-frequency measurements reveal an even larger dispersion between seismic and ultrasonic measurements. The seismic *P*-wave velocity is estimated to be 86–92% of the ultrasonic velocity, with a most likely value of 89%. The dispersion is even higher for vertical Young's modulus, which is estimated to be 67–94% of the ultrasonic Young's modulus, with a most likely value of 80%. Lozovyi & Bauer (2018) observe 20% velocity dispersion in the range from seismic to ultrasonic frequencies for the shaly facies of Opalinus Clay. We observe a dispersion for Opalinus Clay for different facies varying between 13 and 16%. We can infer that Opalinus Clay dispersion is significant even when sourced at different depths and mineralogies.

3.4 Static stiffness—non-elastic effects

The undrained static stiffness is determined from the static undrained triaxial loading-unloading cycle (Table 5). We determine the conventional stiffness from the stress-strain changes of the unloading section with a stress amplitude between 8 and 10 MPa.

Plots of non-elastic compliance as a function of axial stress change have been subject to a former study (Lozovyi *et al.* 2022) to calculate the zero-stress compliance and the respective zero-stress Young's modulus and Poisson's ratio independent of stress amplitude.

The strain rate in our static tests is in the order of 10^{-8}–10^{-7} s^{-1}, which corresponds to an elastic wave with a frequency in the order of 0.01 Hz (Fjær *et al.* 2012, 2013). We compared the zero-stress Young's modulus E_0 with Young's modulus from low-frequency measurements at the strain rate equivalent frequency of 1 Hz, $E_{1\,\mathrm{Hz}}$:

$$\frac{E_0}{E_{1\,\mathrm{Hz}}} = 0.95 \tag{12}$$

showing that E_0 is slightly lower than $E_{1\,\mathrm{Hz}}$. The deviation in zero-stress Poisson's ratio to Poisson's ratio at 1 Hz low-frequency measurement is insignificantly low and within the error.

Fig. 13(a) shows the comparison in Young's modulus assuming isotropy for sonic and ultrasonic velocity measurements with frequency, showing a similar trend as we have seen in Fig. 11. The isotropy assumption is based on a test on an Opalinus Clay twin sample to the sample O2, which is discussed in Section C. A closer look at the comparison between static measurement, zero-stress amplitude method, and low-frequency measurement (Fig. 13b) shows an increase from static Young's modulus to low-frequency Young's modulus that is non-negligible and varies from 9% (F1) to 34% (P2).

3.5 Attenuation

We employed the Cole–Cole relaxation model (Cole & Cole 1941) to align seismic and ultrasonic laboratory measurement data, aiming to forecast stiffness across the entire range of frequencies. The mathematical description of the model is shown in Appendix D. This was particularly aimed towards estimating the laboratory data point for the corresponding sonic logging measurement (Fig. 14). We, therefore, assume a frequency dependence of Young's modulus, as previously discussed. This allows for the comparison between laboratory and sonic well logging data.

Fitting the measurement data to the model includes several constraints: The low-frequency limit modulus was derived from Young's modulus measurements in the seismic frequency range of 0.5–20 Hz, as they encompass a broader range compared to *P*-wave modulus measurements (0.5–2 Hz). The high-frequency limit modulus was determined from ultrasonic Young's modulus, which was converted from *P*- and *S*-wave velocity measurements under the assumption of isotropy. The error of the ultrasonic Young's modulus was weighted to compensate for the number of low-frequency data points. Moreover, E_∞, the maximum Young's modulus at the highest frequency, was limited to 101% of the ultrasonic value at 250 kHz as no larger dispersion is expected within ultrasonic frequencies. Knowing low- and high-frequency limits, the characteristic frequency and the parameter α were determined by the least square fit method. The samples with the lowest clay content, S1 (Fig. 14h) and F1 (Fig. 14i) show no significant attenuation.

In the subsequent step, while transitioning from Young's modulus to *P*-wave modulus and the associated *P*-wave velocity, the parameters f_0 and α were presumed to remain consistent (see Fig. 15). The height of the attenuation peak, however, is not affected by the characteristic frequency and α. The absolute attenuation is also defined by the low- and high-frequency moduli. We, therefore, assume for anisotropic rocks, such as Opalinus Clay, that the vertical Young's modulus and *P*-wave velocity dispersion mechanisms occur in the same frequency range. Given f_0 and α, laboratory-measured *P*-wave data are fitted by the least square method. The laboratory data include seismic *P*-wave moduli and attenuation (0.5–2 Hz) and ultrasonic *P*-wave modulus measurements. Again, the error of the ultrasonic Young's modulus was weighted to compensate for the number of low-frequency data points. Same, as with E_∞, the *P*-wave modulus M_∞ was limited to 101% of the ultrasonic value at 250 kHz.

Eventually, the difference between the modelled laboratory velocities at 20 kHz and sonic well log velocities is determined. The values for the samples O2, O3, W1 and F1 are within a deviation of 3% between the model and sonic well log velocities. The sonic log values for the samples O1, P1, P2 and F2 are below the modelled results. Possible reasons for deviations will be explained in Section 4. Sample S1 has a 7% higher sonic well logging velocity than predicted by the model. Formation S1 is the deepest tested formation, where the effective stress in the formation was likely higher than the effective stress in the laboratory test.

Cross-correlations of the deviation between sonic logging velocities and laboratory measurements with mineralogy, porosity, stiffness, dispersion or velocity fluctuations around the core location do not show a clear trend.

A comparison between the measured ultrasonic velocities and the Cole–Cole model predicted at 20 kHz (sonic well logging velocity) shows little dispersion in the range between 20 and 250 kHz. Sonic velocities are 99 ± 1% of the ultrasonic velocities. This indicates that most relaxation processes occur below sonic frequencies.

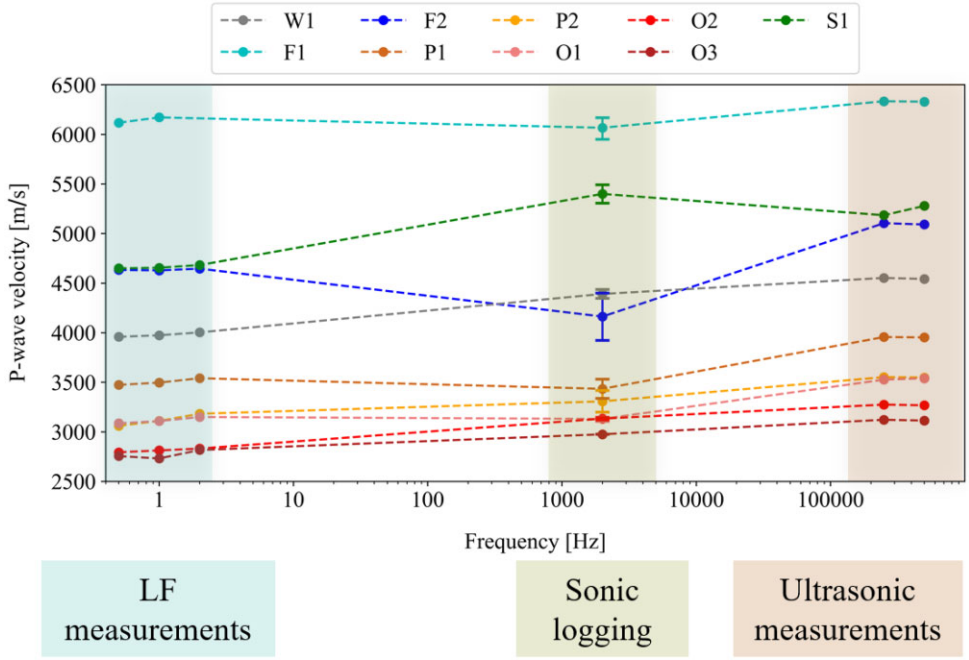

Figure 11. Vertical *P*-wave velocity as a function of frequency shows the laboratory results at seismic and ultrasonic frequencies and the borehole field data at sonic frequencies. At seismic frequencies, *P*-wave velocity has been obtained from direct *P*-wave modulus measurements. The abbreviation *LF* stands for low-frequency. Error bars for the results of sonic logging measurements indicate the standard deviation of the log measurements in a range of ±30 cm around the depth of the laboratory-tested sample.

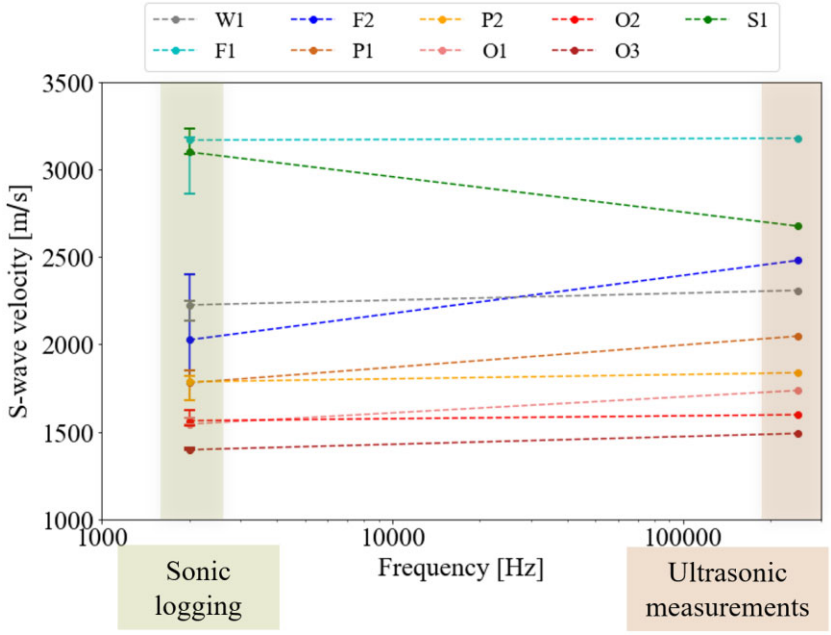

Figure 12. Vertical *S*-wave velocity as a function of frequency shows the borehole field data at sonic frequencies and the laboratory results at ultrasonic frequencies. Error bars for the results of sonic logging measurements indicate the standard deviation of the log measurements in a range of ±30 cm around the depth of the laboratory-tested sample. Low-frequency data is not available at seismic frequencies.

4 DISCUSSION

4.1 Dispersion in experimental data

The laboratory tests give insight into the comparison between laboratory and field measurements at different frequencies. Continuous quantitative information of elastic properties in boreholes can only be derived from dynamic measurements, and therefore a conversion factor must be applied to derive static elastic properties for, for example design of underground structures. That conversion factor may account for different processes (Fjær 2019) and may also be markedly different for different lithologies. The study's particular interest was to examine the potential effect of clay mineral content (as a proxy) on such a conversion factor and examine this not only

Table 5. Stress and strain rates during undrained static triaxial loading in the upper part of the table and strains at the end of the consolidation segment in the lower part of the table.

Sample ID	W1	F1	F2	P1	P2	O1	O2	O3	S1
Stress rate [MPa/ hr]	3.5	3.6	3.5	3.6	3.6	2.6	2.7	2.7	3.6
Strain rate [m/m m/ hr]	0.16	0.052	0.11	0.21	0.31	0.21	0.29	0.27	0.085
Axial LVDT strain [mm/ m]	−1.58	0.12	−0.72	−0.88	−1.31	−1.54	−3.14	−3.18	0.25
Axial strain gauge strain [mm /m]	−1.96	−0.23	−0.65	−1.03	−1.46	−2.29	−3.37	−3.98	0.09
Radial strain gauge strain [mm/ m]	−0.46	0.78	−0.24	0.16	0.18	−0.11	−0.50	−0.29	0.59
Volumetric strain gauge strain [mm/ m]	−2.88	1.33	−1.13	−0.71	−1.10	−2.51	−4.37	−4.56	1.26

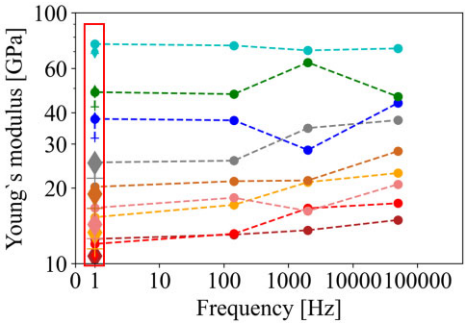

(a) We made the assumption of isotropic media to compute Young's moduli at sonic and ultrasonic frequencies.

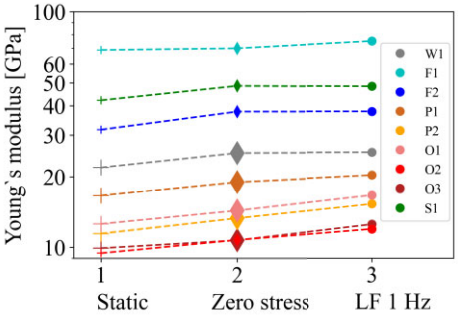

(b) At 1 Hz, we show the static (1), zero-stress amplitude (2), and low-frequency 1 Hz (3) Young's moduli measurement results in a close-up.

Figure 13. Young's modulus versus frequency: The left plot shows a close-up of the red box on the left-hand side figure. Colours indicate the nine tested samples, whereas the colour code remains the same as in all previous plots.

empirically but also to understand the governing processes of potential differences. This shall improve geomechanical models of the subsurface.

The low-frequency measurements reveal that the material's stiffness increases with decreasing clay content (Fig. 16a). This is commonly observed in rocks where clay contributes to the load-bearing phase (Lozovyi *et al.* 2022). We moreover observed a positive correlation between clay content and the degree of dispersion (Fig. 16b). If we normalize the results to Young's modulus to the value measured at 0.5 Hz (Fig. 9b), however, we see that the seismic dispersion for the samples with a high clay content is as high as 13% (sample P2). The samples F1, F2 and S1 (lowest clay content from 1 to 10 wt.%) show a slightly negative dispersion of up to −1%. This is within the experimental error and cannot be reasonably explained by physical mechanisms in the rock itself. We could not detect dispersion for the Poisson's ratio within the seismic frequency band. This can be explained by dominating fluid effects since we performed the tests under undrained conditions.

It is essential to note that the transition from the drained to undrained state happens at low frequencies and leads to dispersion as previously mentioned (Pimienta *et al.* 2015a). In this study, we chose the boundary conditions in a way that the elastic properties are directly undrained so that this transition can be discarded. The dead volume of the system is 2 ml, which is sufficiently small to restrict drainage effects (Lozovyi & Bauer 2019a). For measurements on shale samples, the permeability is, in addition, low enough so that there is no significant fluid flow out of the sample's boundaries Szewczyk *et al.* (2016). Another observation is that samples with very small clay content (S1, F1 and F2) do not show seismic frequency dispersion with a transition from drained to undrained conditions, as the tests show only undrained results.

While the low-frequency to ultrasonic measurements show a clear increasing trend with increasing frequency (Fig. 11), the comparison to sonic logging data is not trivial. We, therefore, show error intervals for the sonic logging measurement fluctuations that are ±30 cm around the depth of the lab sample using the standard deviation method. The exact location might be slightly shifted relative to the recorded logging depth. A larger difference is here also the resolution, which is about 5 cm core size for the laboratory samples, and between 1 and 2 m set by the distance between transmitting and receiving transducers during sonic logging. This plays a significant role in heterogeneous sections, where the rock properties change over a short distance. Potential fractures within the formation can also contribute to diminished sonic logging velocities. However, for laboratory measurements, we selectively utilize core samples that do not exhibit larger fractures.

Considering these uncertainties, we find the sonic velocities in the range between seismic and ultrasonic velocities, as one would expect. An exception is sample S1, which has a significantly higher sonic velocity than the ultrasonic velocity. An explanation for that can be that S1 is our stratigraphically deepest sample with a sample depth of 1101.10 m (see Table 1) with in situ stresses likely higher than used in the laboratory. Moreover, sample S1 shows a strong fluctuation of logging properties (see Fig. 4). Another possible reason for observed differences between log data and laboratory results is that if we drill the samples from the preserved cores (Section 2.2), we avoid parts with cracks and inhomogeneities as we measure the elastic properties only along a short distance (about 5 cm). In the field, however, the averaged signal is measured along a distance that is 20 times larger. The opposite to S1 observation is found for F2, where the sonic logging velocities are significantly lower. We believe this is the consequence of a nearby fracture visible on a CT scan of the core.

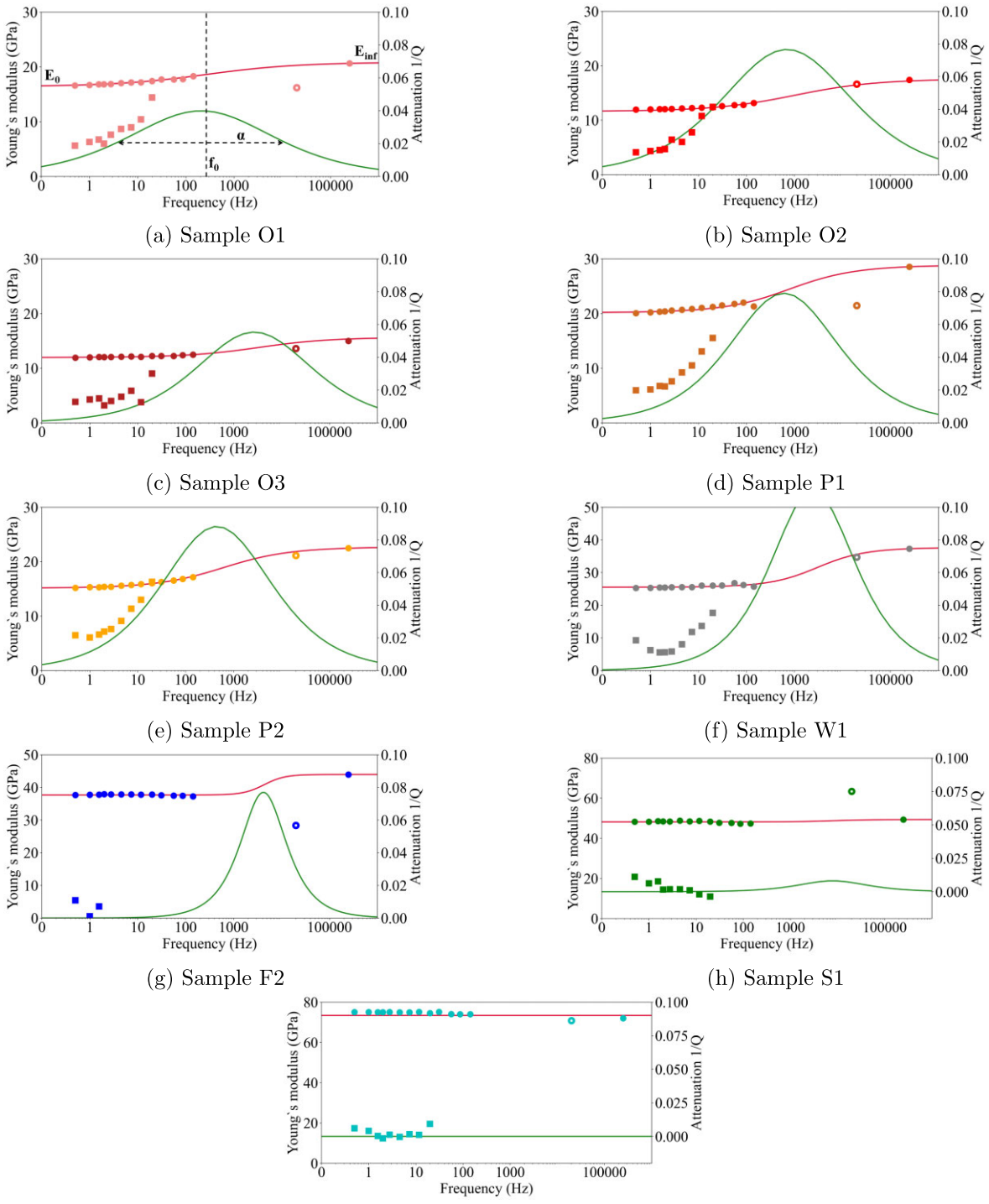

Figure 14. Cole–Cole model (Cole & Cole 1941) fitted to laboratory Young's modulus and attenuation measurements at seismic frequencies and converted Young's modulus at ultrasonic frequencies. We therefore have to assume isotropy which may lead to about 5% error. Fig. 14(a) shows the low-frequency limit E_0, the high-frequency limit E_∞, the characteristic frequency f_0 and the parameter α (width of the relaxation time distribution). The red line shows the modelled distribution of Young's modulus as a function of frequency, and the green line the modelled attenuation as a function of frequency. Closed circles indicate laboratory measurement data of Young's modulus (converted at ultrasonic frequencies), open circles sonic well logging measurements and squares attenuation measurements at seismic frequencies.

Overall, the experimental results show dispersion in measured Young's modulus within the low frequency (0.5–143 Hz) regime (Fig. 9) and further between low and ultrasonic frequencies (Fig. 14). This obviously implies *P*-wave velocity dispersion, as illustrated in Fig. 11 and in Fig. 15. The low-frequency dispersion is particularly visible in clay-rich samples, accompanied by increasing attenuation. The model of Cole & Cole (1941) (Section 3.5) considers only one transition frequency, whereas several relaxation mechanisms can

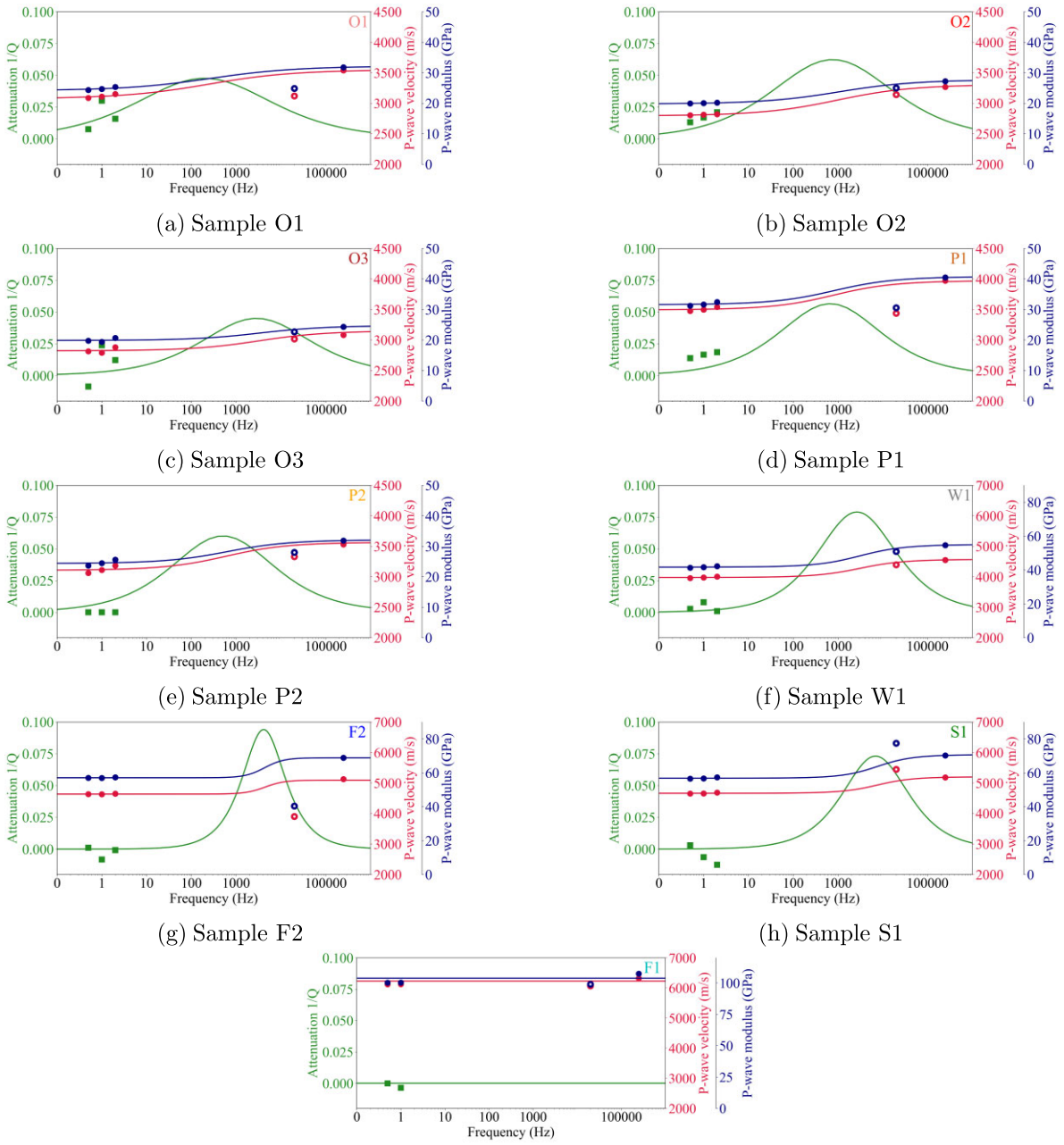

Figure 15. Cole–Cole model (Cole & Cole 1941) fitted to laboratory *P*-wave modulus, *P*-wave velocity and attenuation measurements at seismic frequencies. The red line shows the modelled distribution of *P*-wave velocity, the blue line the modelled *P*-wave modulus and the green line the modelled attenuation as a function of frequency. Closed red circles indicate laboratory measurement data of *P*-wave modulus, closed blue circles show laboratory measurement data of *P*-wave velocity, open circles (red and blue) sonic well logging measurements, and squares attenuation measurements at seismic frequencies.

control the overall dispersion simultaneously, as we will show in the following, where we discuss possible dispersion mechanisms in the clay and non-clay phase.

4.2 Viscoelastic bound water in the clay phase

Several observations of low-frequency dispersion in clay and shale have been published. Shale data obtained with forced oscillator techniques as applied here show dispersion in the seismic frequency range accompanied by strong dispersion between seismic and ultrasonic frequencies (Duranti *et al.* 2005; Szewczyk *et al.* 2018a; Lozovyi & Bauer 2019b). Mainsant *et al.* (2012) measured strong frequency dependence of the shear modulus in pure quick clay close to the liquid limit. The measured shear modulus increased by approximately one order of magnitude from 0.1 to 10 Hz (still very low: 10^4–10^5 Pa), showing viscoelastic behaviour in close agreement with a Maxwell model. The source of such dispersion may be found in the viscoelastic behaviour of water near solid surfaces, as described in Section 1.

Holt & Fjær (2003), Holt & Kolstø (2017) and Sayers & den Boer (2018) present models to determine the elastic properties of clay minerals in shales, where they take bound water and inter-particle

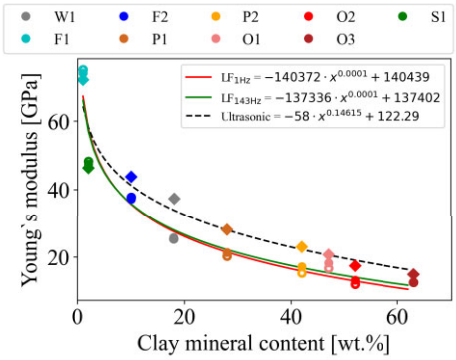

(a) Open circles indicate LF measurements at 0.5 Hz, closed circles at 143 Hz, whereas diamonds show the results at ultrasonic frequencies. R^2 for LF at 1 Hz and 143 Hz (red, green curve) is 0.96, and for ultrasonic velocities (black curve) is 0.89 for a power law fit, respectively.

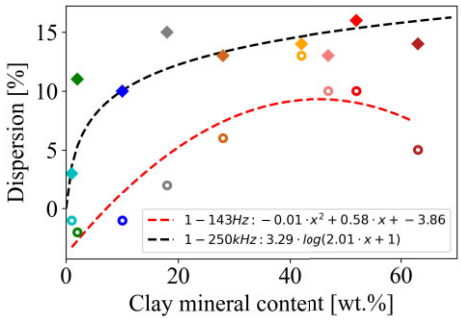

(b) Open circles indicate averaged LF measurements from 0.5 Hz to 143 Hz, and diamonds show the results at ultrasonic frequencies. R^2 from 1-143 Hz (red curve) is 0.83 for the polynomial fit, and from 1-250 kHz (black curve) is 0.71 for the logarithmic fit.

Figure 16. Correlation between Young's modulus (a) and dispersion (b) within the seismic frequency band and for ultrasonic frequencies with clay mineral content.

contacts into consideration. Batzle *et al.* (2005) point out that fluid motion in shales is constrained and that particle interaction with bound water may be a controlling mechanism for dispersion. This was confirmed by experimental studies of Szewczyk *et al.* (2018a), who found a substantial increase in dispersion with increasing water saturation and attributed this behavior to local flow possibly involving bound water. Thus, such adsorbed or bound water on clay mineral surfaces within narrow (nanometer scale) pores and inside clay minerals represents a likely dispersion mechanism in clay-rich rocks (Holt & Kolstø 2017). According to the Maxwell model, the transition frequency is proportional to the ratio of the high-frequency limit of the bound water shear modulus and the bound water viscosity. This frequency easily falls into the low-frequency band. Previous works pointing to the impact of bound water on the elastic properties of shale include Sayers & den Boer (2018), Gelinsky (2020) and Asaka *et al.* (2021).

The clay mineralogy, especially swelling clay minerals such as smectite, plays a decisive role (see Fig. 3). It shows that illite is the dominant clay mineral, follzowed by kaolinite. Sample W1 contains the largest amounts of the swelling mineral smectite, with about 11%.

We used specific surface area measurements from nitrogen adsorption (BET) analysis to estimate the volume fraction of bound water in the pore space (Holt & Kolstø 2017):

$$f_{\mathrm{bw}} = \delta_{\mathrm{H_2O}} S_g \rho_s \frac{1-\phi}{\phi}, \tag{13}$$

where $\delta_{\mathrm{H_2O}}$ is thickness of a water monolayer (~0.25 nm), S_g is the specific surface area in $\mathrm{m^2\ g^{-1}}$, ρ_s is the solid material density and ϕ is porosity.

Fig. 17 shows the measured specific surface area and the volume fraction of bound water in the pore space calculated from Holt & Kolstø (2017) as a function of clay mineral content. The specific surface area increases with increasing clay content, demonstrating that the specific surface area must be related to bound water. Sample W1 shows a large volume fraction of bound water compared to the relative clay mineral content. It is much higher than, for example, sample O3, which has a significantly higher clay content. However, sample W1 contains more than twice as much swelling clay minerals, such as smectite, compared to sample O3. This leads to a higher volume fraction of bound water.

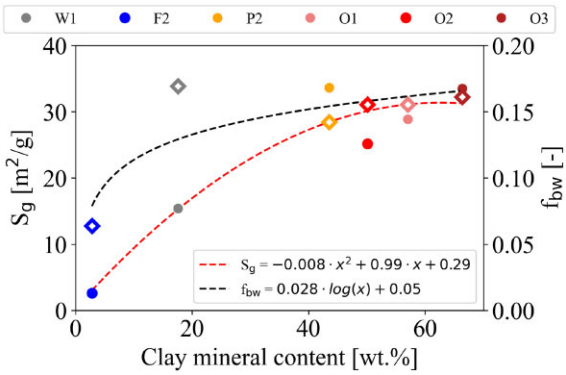

Figure 17. Specific surface area (circles) and volume fraction of bound water in the pore space (diamonds, see eq. 13) versus clay content. The red dashed line shows a polynomial fit ($R^2 = 0.92$) for the specific surface area, and the black dashed line a logarithmic fit ($R^2 = 0.73$) for the volume fraction of bound water in the pore space. Colours indicate the nine tested samples, whereas the colour code remains the same as in all previous plots.

4.3 Micromechanical model

We analyse the experimental data above with a simplistic rock physics model (see Appendix E for mathematical description and choice of parameters), considering 'clay' and 'non-clay' as two ingredients of our effective medium.

Comparisons between modelled and measured Young's modulus are shown in Fig. 18 for frequencies 0.5 and 143 Hz. The model captures the decreasing stiffness with increasing clay content and also the differences between the moduli at different frequencies.

Fig. 19 shows modelled *P*-wave velocity, measured *P*-wave velocity at 0.5 Hz and directly measured *P*-wave velocity at 250 kHz. The velocity also shows a significant decrease with increasing clay content. The dispersion between low and ultrasonic frequencies is much larger than seen within the low-frequency window only (Fig. 18).

Fig. 20 shows the frequency-dependent Young's modulus computed for sample O3, along with laboratory data and the derived value from log data at 20 kHz. In this case, a few parameters were adjusted: The main point of showing this figure is not to state how

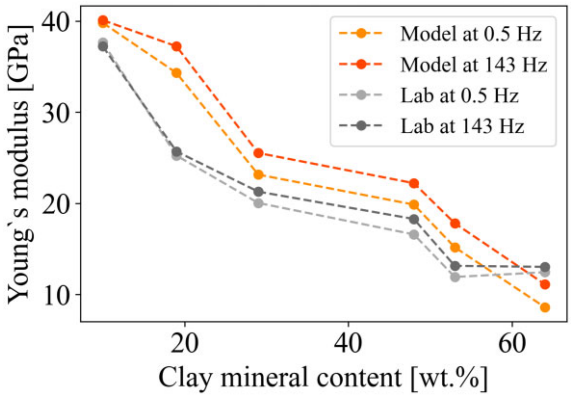

Figure 18. Young's modulus versus clay content for the laboratory and modelled data at 0.5 and 143 Hz.

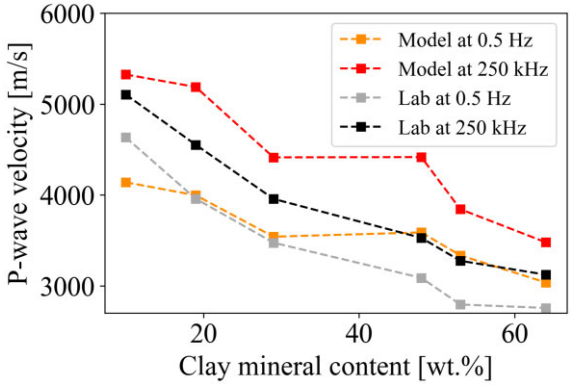

Figure 19. *P*-wave velocity versus clay content for the laboratory and modelled data at 0.5 Hz and 250 kHz. The solid phase density in the modelled data is likewise a weighted average of the densities of non-clay (see Table 1) minerals composing each sample.

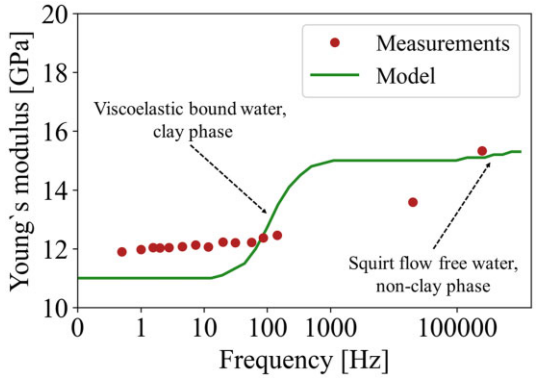

Figure 20. Young's modulus versus frequency for sample O3. The simplified model indicates two dispersion mechanisms: (i) viscoelastic bound water in the clay phase with a transition frequency of 150 Hz and (ii) squirt flow free water in the non-clay phase with a transition frequency near 200 kHz.

well the model fits the data but rather to point to two possible dispersion mechanisms: Viscoelastic bound water in the clay phase, with a transition frequency near 100 Hz, and squirt flow of free water in the non-clay phase, with transition frequency near 800 kHz. Of course, these transitions may be shifted based on more information about microtexture and, if possible, measurements at more frequencies between 150 Hz and 100 kHz. Note also that actual transitions appear sharper in the simplified model and will be smeared out by heterogeneities in the rock samples. Low-frequency dispersion may also be inferred by squirt and viscous shear relaxation of the bound water itself, but preliminary analysis indicates that these would contribute little to the observed dispersion. Finally, dispersion could be caused by patchiness in saturation or in material properties, but given the low permeability, the associated transition frequency on the core sample scale would be well below 1 Hz.

Based on the dispersion mechanisms described in Section 1, we conclude that the most likely causes of observed dispersion in the samples studied here are bound water viscoelasticity associated with clay minerals and possibly free water squirt associated with the non-clay components. We cannot discard the effects of bound water squirt, and we have no reason to expect patchiness effects since the samples were fully saturated. Obviously, rigorous rock physics modelling of these effects is not feasible because we do not have sufficient input data. We may, however, see to what extent our assumptions and hypotheses may produce results that are aligned. Further work is required, both in the laboratory and on modelling, to paint the complete picture of dispersive wave velocities in composite shale-like materials.

5 CONCLUSION

This research gives insight into the role of frequency in measured elastic parameters by comparing static compression and dynamic stiffness measurements at seismic and ultrasonic frequencies to well logging data.

It reveals a consistent trend of increasing velocities with frequency, with *P*-wave dispersion varying from 3 to 16% between 1 Hz and 500 kHz. The study also finds that increased clay content correlates with decreased stiffness, both static and dynamic.

A notable distinction is observed between static Young's modulus and dynamic low-frequency Young's modulus, with the dynamic values being 34% higher due to finite strain effects. The higher dispersion seen with increased clay content is potentially linked to the influence of bound water, suggesting a key role in dispersion.

In conclusion, this study provides a comprehensive data set that lays the groundwork for enhancing the conversion from dynamic to static stiffness. This data set can be leveraged to develop a model that is calibrated with the results of this work, incorporating dispersion mechanisms. Such a model will make use of well logging information, allowing it to account for the dispersion-related impacts of clay mineral content. This approach will offer more accurate and reliable interpretations for geomechanical applications.

ACKNOWLEDGMENTS

This work was performed in SINTEF's Formation Physics laboratory and was funded by the Nationale Genossenschaft für die Lagerung radioaktiver Abfälle (nagra) in Switzerland. The authors also acknowledge funding from the Research Council of Norway through PETROMAKS 2 program researcher project (grant #301910) at SINTEF: Calibrated rock physics model for quantitative seismic analysis of two-phase fluid saturation. Martin Mazurek (RWI, University of Bern, Switzerland) is acknowledged for providing data on the mineralogy of the tested samples, and Rodney Garrard (nagra) for processing of logging data.

DATA AVAILABILITY

All experimental measurements are available upon request from the corresponding author.

REFERENCES

Alkhimenkov, Y., Caspari, E., Gurevich, B., Barbosa, N.D., Glubokovskikh, S., Hunziker, J. & Quintal, B., 2020. Frequency-dependent attenuation and dispersion caused by squirt flow: three-dimensional numerical study, *Geophysics,* **85**(3), MR129–MR145.

Antognozzi, M., Humphris, A.D. & Miles, M.J., 2001. Observation of molecular layering in a confined water film and study of the layers viscoelastic properties, *Appl. Phys. Lett.,* **78**(3), 300–302.

Asaka, M., Holt, R.M. & Bakk, A., 2021. Rock physics model of shale: predictive aspect, *J. geophys. Res.,* **126**(9) , doi:10.1029/2021JB021993.

Batzle, M. & Wang, Z., 1992. Seismic properties of pore fluids, *Geophysics,* **57**(11), doi:10.1190/1.1443207.

Batzle, M., Hofmann, R., Prasad, M., Kumar, G., Duranti, L. & Han, D.H., 2005. Seismic attenuation: observations and mechanisms, in *Society of Exploration Geophysicists - 75th SEG International Exposition and Annual Meeting, SEG 2005,* pp. 1565–1568, Society of Exploration Geophysicists.

Batzle, M.L., Han, D.H. & Hofmann, R., 2006. Fluid mobility and frequency-dependent seismic velocity - direct measurements, *Geophysics,* **71**(1), doi:10.1190/1.2159053.

Best, A.I. & McCann, C., 1995. Seismic attenuation and pore-fluid viscosity in clay-rich reservoir sandstones, *Geophysics,* **60**(5), 1386–1397.

Bossart, P. *et al.*, 2017. Mont Terri rock laboratory, 20 years of research: introduction, site characteristics and overview of experiments, *Swiss J. Geosci.,* **110**(1), 3–22.

Bourg, I.C., 2015. Sealing shales versus brittle shales: a sharp threshold in the material properties and energy technology uses of fine-grained sedimentary rocks, *Environ. Sci. Technol. Lett.,* **2**(10), 255–259.

Budiansky, B. & O'connell, R.J., 1976. Elastic moduli of a cracked solid, *Int. J. Solids Struct.,* **12**(2), 81–97.

Chapman, M., 2003. Frequency-dependent anisotropy due to meso-scale fractures in the presence of equant porosity, *Geophys. Prospect.,* **51,** 369–379.

Chapman, S., Quintal, B., Tisato, N. & Holliger, K., 2017. Frequency scaling of seismic attenuation in rocks saturated with two fluid phases, *Geophys. J. Int.,* **208**(1), 221–225.

Cole, K.S. & Cole, R.H., 1941. Dispersion and absorption in dielectrics I. Alternating current characteristics, *J. Chem. Phys.,* **9**(4), 341–351.

Colten-Bradley, V.A., 1987. Role of pressure in smectite dehydration–effects on geopressure and smectite-to-illite transformation, *AAPG Bull.,* **71**(11), 1414–1427.

Crisci, E., Giger, S. & Laloui, L., 2021. TBO Trüllikon-1-1: Data Report. Dossier IX: Rockmechanical and geomechanical laboratory testing, Nagra Arbeitsbericht NAB 20-09.

Dumon, M. & Van Ranst, E., 2016. PyXRD v0.6.7: a free and open-source program to quantify disordered phyllosilicates using multi-specimen X-ray diffraction profile fitting, *Geosci. Model Dev.,* **9**(1), 41–57.

Duranti, L., Ewy, R. & Hofmann, R., 2005. Dispersive and attenuative nature of shales: Multiscale and multifrequency observations, in *Society of Exploration Geophysicists - 75th SEG International Exposition and Annual Meeting, SEG 2005,* pp. 1577–1580, Society of Exploration Geophysicists.

Fjær, E., 2019. Relations between static and dynamic moduli of sedimentary rocks, *Geophys. Prospect.,* **67**(1), 128–139.

Fjær, E., Holt, R.M., Nes, O.-M. & Stenebråten, J.F., 2011. The transition from elastic to non-elastic behavior, in *Paper presented at the 45th U.S. Rock Mechanics / Geomechanics Symposium,* 26–29 June 2011, San Francisco, CA, USA, Paper Number: ARMA-11-389, American Rock Mechanics Association.

Fjær, E., Stroisz, A.M. & Holt, R.M., 2012. Combining static and dynamic measurements for evaluation of elastic dispersion, in *Paper presented at the 46th U.S. Rock Mechanics/Geomechanics Symposium,* 24–27 June 2012, Chicago, IL, USA, Paper Number: ARMA-2012-537, American Rock Mechanics Association.

Fjær, E., Stroisz, A.M. & Holt, R.M., 2013. Elastic dispersion derived from a combination of static and dynamic measurements, *Rock Mech. Rock Eng.,* **46**(3), 611–618.

Fjær, E., Holt, R.M., Horsrud, P. & Raaen, A.M., 2021. *Petroleum Related Rock Mechanics,* Vol. **53,** 3rd edn, Elsevier Science.

Gassmann, F., 1951. Über die Elastizität poröser Medien, *Vierteljahrschrift der Naturforschenden Gesellschaft in Zürich,* pp. 1–23.

Gelinsky, S., 2020. Reservoir characterization supported by rock physics diagnostics, in *Paper presented at the Offshore Technology Conference Asia,* 2–6 November 2020, Kuala Lumpur, Malaysia, Paper Number: OTC-30359-MS, pp. 1–10.

Ghabezloo, S. & Sulem, J., 2010. Effect of the volume of the drainage system on the measurement of undrained thermo-poro-elastic parameters, *Int. J. Rock Mech. Min. Sci.,* **47**(1), 60–68.

Goldberg, D. & Zinszner, B., 1989. P-wave attenuation measurements from laboratory resonance and sonic waveform data, *Geophysics,* **54**(1), 76–81.

Gonus, J., Bailey, E., Desroches, J. & Garrard, R., 2021. TBO Trüllikon-1-1: Data Report. Dossier VI: Wireline Logging and Micro-hydraulic Fracturing, Nagra Arbeitsbericht NAB 20-09.

Holt, R.M. & Fjær, E., 2003. Wave velocities in shales - a rock physics model, in *Proceedings of the EAGE 65th Conference & Exhibition,* 2–5 June 2003, Stavanger, Norway.

Holt, R.M. & Kolstø, M.I., 2017. How does water near clay mineral surfaces influence the rock physics of shales?, *Geophys. Prospect.,* **65**(6), 1615–1629.

Holt, R.M., Bauer, A., Bakk, A. & Szewczyk, D., 2016. Stress path dependence of ultrasonic and seismic velocities in shale, in *SEG Technical Program Expanded Abstracts,* Vol. **35,** pp. 3159–3163, Society of Exploration Geophysicists.

Hughes, D.S., Pondrom, W.L. & Mims, R.L., 1949. Transmission of elastic pulses in metal rods, *Phys. Rev.,* **75**(10), 1552–1556.

Hüpers, A. & Kopf, A.J., 2012. Effect of smectite dehydration on pore water geochemistry in the shallow subduction zone: an experimental approach, *Geochem. Geophys. Geosyst.,* **13**(1) , doi:10.1029/2012GC004212.

Jackson, I., Paterson, M.S., Niesler, H. & Waterford, R.M., 1984. Rock anelasticity measurements at high pressure, low strain amplitude and seismic frequency, *Geophys. Res. Lett.,* **11**(12), 1235–1238.

Jones, T.D., 1986. Pore fluids and frequency-dependent wave propagation in rocks, *Geophysics,* **51**(10), 1939–1953.

Jordan, P., Naef, H., Schürch, P., Schwarz, M., Ibele, T., Felber, R. & Gysi, M., 2021. TBO Bülach-1-1: Data Report. Dossier III: Lithostratigraphy, Nagra Arbeitsbericht NAB 20-08.

Lozovyi, S. & Bauer, A., 2018. Static and dynamic stiffness measurements with Opalinus Clay, *Geophys. Prospect.,* **67**(4), 997–1019.

Lozovyi, S. & Bauer, A., 2019a. Velocity dispersion in rocks: a laboratory technique for direct measurement of P-wave modulus at seismic frequencies, *Rev. Sci. Instrum.,* **90**(2) , doi:10.1063/1.5026969.

Lozovyi, S. & Bauer, A., 2019b. From static to dynamic stiffness of shales: frequency and stress dependence, *Rock Mech. Rock Eng.,* **52**(12), 5085–5098.

Lozovyi, S., Sirevaag, T., Szewczyk, D., Bauer, A. & Fjær, E., 2017. Non-elastic effects in static and dynamic rock stiffness, in *Paper presented at the 51st U.S. Rock Mechanics/Geomechanics Symposium,* 25–28 June 2017, San Francisco, CA, USA, Paper Number: ARMA-2017-0293, American Rock Mechanics Association.

Lozovyi, S., Bauer, A., Giger, S. & Chakraborty, S., 2018. Static vs. dynamic stiffness of shales: frequency and stress effects, in *Paper presented at the 52nd U.S. Rock Mechanics/Geomechanics Symposium,* co7–20 June 2018, Seattle, WA, USA, Paper Number: ARMA-2018-257, American Rock Mechanics Association.

Lozovyi, S., Mews, K.S., Fjær, E. & Giger, S., 2022. How static stiffness is affected by non-elastic deformations in different lithologies, in *Paper presented at the 56th U.S. Rock Mechanics/Geomechanics Symposium,* 26–29 June 2022, Santa Fe, NM, USA, Paper Number: ARMA-2022-0714, American Rock Mechanics Association.

Mainsant, G., Jongmans, D., Chambon, G., Larose, E. & Baillet, L., 2012. Shear-wave velocity as an indicator for rheological changes in clay materials: Lessons from laboratory experiments, *Geophys. Res. Lett.,* **39**(19) , doi:10.1029/2012GL053159.

Marion, D.P. & Coudin, P., 1992. Fram ray to effective medium theories in stratified media: an experimental study, in *SEG Technical Program Expanded Abstracts 1992,* pp. 1341–1343, Society of Exploration Geophysicists.

Marketos, G. & Best, A.I., 2010. Application of the BISQ model to clay squirt flow in reservoir sandstones, *J. geophys. Res.,* **115**(6) , doi:10.1029/2009JB006495.

Mavko, G., Mukerji, T. & Dvorkin, J., 2009. *The Rock Physics Handbook,* Cambridge Univ. Press.

Mavko, G.M. & Nur, A., 1978. Effect of nonelliptical cracks on the compressibility of rocks, *J. geophys. Res.,* **83**(B9), 4459–4468.

Mazurek, M. *et al.*, 2023. Swiss deep drilling campaign 2019-2022:geological overview and rock properties with focus on porosity and pore geometry, *Appl Geochem.,* **159,** doi:10.1016/j.apgeochem.2023.105839.

Mikhaltsevitch, V. & Lebedev, M., 2014. A laboratory study of low-frequency wave dispersion and attenuation in water-saturated sandstones, *Leading Edge,* **33**(6), 589–696.

Mikhaltsevitch, V., Lebedev, M., Chavez, R., Vargas, E.A. & Vasquez, G.F., 2021a. A laboratory forced-oscillation apparatus for measurements of elastic and anelastic properties of rocks at seismic frequencies, *Front. Earth Sci.,* **9** , doi:10.3389/feart.2021.654205.

Mikhaltsevitch, V., Lebedev, M., Pervukhina, M. & Gurevich, B., 2021b. Seismic dispersion and attenuation in Mancos shale – laboratory measurements, *Geophys. Prospect.,* **69**(3), 568–585.

Moos, D. & Zoback, M.D., 1983. In situ studies of velocity in fractured crystalline rocks, *J. geophys. Res.,* **88**(B3), 2345–2358.

Murphy, W.F., 1982. Effects of partial water saturation on attenuation in Massilon sandstone and Vycor porous glass, *J. acoust. Soc. Am.,* **71**(6), 1458–1468.

Murphy, W.F., Winkler, K.W. & Kleinberg, R.L., 1986. Acoustic relaxation in sedimentary rocks: dependence on grain contacts and fluid saturation., *Geophysics,* **51**(3), 757–766.

Nur, A., Mavko, G., Dvorkin, J. & Galmudi, D., 1998. Critical porosity: a key to relating physical properties to porosity in rocks, *Leading Edge,* **17**(3), 357, doi:10.1190/1.1437977.

O'Connell, R.J. & Budiansky, B., 1977. Viscoelastic properties of fluid-saturated cracked solids, *J. geophys. Res.,* **82**(36), 5719–5735.

Pimienta, L., Fortin, J. & Guéguen, Y., 2015a. Experimental study of young's modulus dispersion and attenuation in fully saturated sandstones, *Geophysics,* **80**(5), L57–L72.

Pimienta, L., Fortin, J. & Guéguen, Y., 2015b. Bulk modulus dispersion and attenuation in sandstones, *Geophysics,* **80**(2), D111–D127.

Rivière, J. *et al.*, 2016. Frequency, pressure, and strain dependence of nonlinear elasticity in Berea Sandstone, *Geophys. Res. Lett.,* **43**(7), 3226–3236.

Rørheim, S., 2022. *On frequency-dependent rock experiments: A Comparative Review,* ArXiv. /abs/2208.03795.

Rørheim, S., Bauer, A. & Holt, R.M., 2022. On the low-frequency elastic response of Pierre Shale during temperature cycles, *J. geophys. Int.,* **228**(2), 1260–1280.

Sayers, C.M. & den Boer, L.D., 2018. The elastic properties of clay in shales, *J. geophys. Res.,* **123**(7), 5965–5974.

Schwarz, M., Jordan, P., Schürch, P., Naef, H., Ibele, T., Felber, R. & Gysi, M., 2021. TBO Trüllikon-1-1: Data Report. Dossier III: Lithostratigraphy, Nagra Arbeitsbericht NAB 20-09.

Sørensen, M.K. & Fabricius, I.L., 2017. Clay squirt: local flow dispersion in shale-bearing sandstones, *Geophysics,* **82**(1), MR51–MR63.

Spencer, J.W., 1981. Stress relaxations at low frequencies in fluid-saturated rocks: attenuation and modulus dispersion., *J. geophys. Res.,* **86**(B3), 1803–1812.

Spencer, J.W. & Shine, J., 2016. Seismic wave attenuation and modulus dispersion in sandstones, *Geophysics,* **81**(3), doi:10.1190/geo2015-0342.1.

Suarez-Rivera, A., Wilson, R. & Nakagawa, S.M., 2001. Frequency scaling for evaluation of shale and mudstone properties from accoustic velocities, in *Proceedings of the American Geophysical Union, Fall Meeting 2001,* abstract id. T32E-0924, AGU.

Szewczyk, D., Bauer, A. & Holt, R.M., 2016. A new laboratory apparatus for the measurement of seismic dispersion under deviatoric stress conditions, *Geophys. Prospect.,* **64**(4), 789–798.

Szewczyk, D., Holt, R.M. & Bauer, A., 2018a. The impact of saturation on seismic dispersion in shales - laboratory measurements, *Geophysics,* **83**(1), MR15–MR34.

Szewczyk, D., Holt, R.M. & Bauer, A., 2018b. Influence of subsurface injection on time-lapse seismic: laboratory studies at seismic and ultrasonic frequencies, *Geophys. Prospect.,* **66,** 99–115.

Thomsen, L., 1986. Weak elastic anisotropy, *Geophysics,* **51**(10), 1954–1966.

Tisato, N. & Madonna, C., 2012. Attenuation at low seismic frequencies in partially saturated rocks: measurements and description of a new apparatus, *J. appl. Geophys.,* **86,** 44–53.

Tutuncu, A.N., Podio, A.L., Gregory, A.R. & Sharma, M.M., 1998. Nonlinear viscoelastic behavior of sedimentary rocks, Part I: effect of frequency and strain amplitude, *Geophysics,* **63**(1), 184–194.

Winkler, K., Nur, A. & Gladwin, M., 1979. Friction and seismic attenuation in rocks, *Nature,* **277,** 528–531.

Yurikov, A., Lebedev, M., Pervukhina, M. & Gurevich, B., 2019. Water retention effects on elastic properties of Opalinus shale, *Geophys. Prospect.,* **67**(4), 984–996.

Zhu, Y. & Granick, S., 2001. Viscosity of interfacial water, *Phys. Rev. Lett.,* **87**(9), doi:10.1103/PhysRevLett.87.096104.

APPENDIX A: CORRESPONDING DATA

Table A1 shows the measurement results in numbers.

APPENDIX B: EXPERIMENTAL ISSUES

We were facing some experimental issues during the tests: A small continuous reduction in pore pressure in all tests was seen at undrained conditions. We believe this could be due to an undetected leakage. No leakages at undrained conditions were observed during calibration tests with PEEK (Polyether ether ketone) and Aluminium samples. Further, a radial strain drift was detected during the F2 test. The cause might be the partial electrical grounding of the strain gauges with the pore fluid. It did not affect the dynamic measurements, only the static measurement of radial strain. Another effect on the results might be caused by the disintegration along the bedding plane during the mounting of sample O3. The cause for this might be a fracture or a weak plane. We put the sample carefully together and continued mounting. The fracture was outside the active strain gauge part and did not affect the low-frequency measurements. We believe the effect on the ultrasonic velocities is negligible since the rock was tested under stress.

APPENDIX C: ANISOTROPY CHARACTERIZATION

As part of a different study (Crisci *et al.* 2021), experiments were performed on three twin samples to sample O2 (further referred to as $O2_{TI}$) with a full anisotropic description through triaxial tests on differently oriented cores with respect to the bedding plane (Fig. A1). The major difference is that those tests were done using consolidation and strain-controlled loading.

Measuring samples in three different orientations allows for computing the full stiffness matrix from ultrasonic velocities in 0°-, 60°- and 90°-orientation for transversely isotropic media (TI) with

Table A1. Summary of all measured, modelled and well logging data.

Sample ID	W1	F1	F2	P1	P2	O1	O2	O3	S1
Clay mineral content [wt.%]	18	1	10	28	42	47	52	63	2
Elastic parameters									
E [GPa], LF at 0.5 Hz	25.25	75.05	37.67	20.05	15.17	16.60	11.93	11.90	48.23
E [GPa], LF at 143 Hz	25.71	73.99	37.24	21.29	17.14	18.29	13.15	12.46	47.38
Dispersion E (0.5–143 Hz) [%]	2	−1	−1	6	13	10	10	5	-2
PR [-], LF at 0.5 Hz	0.32	0.30	0.31	0.32	0.30	0.34	0.31	0.28	0.26
PR [-], LF at 143 Hz	0.31	0.30	0.31	0.32	0.30	0.34	0.31	0.27	0.28
Dispersion PR (0.5–143 Hz) [%]	−3	0	0	−1	-2	0	−1	−2	7
Attenuation $1/Q$, LF at 0.5 Hz	0.019	0.006	0.011	0.02	0.022	0.019	0.014	0.013	0.011
Attenuation $1/Q$, LF at 20 Hz	0.035	0.009	N/A	0.052	0.054	0.048	0.041	0.030	−0.004
Velocities at $p_c = 15$ MPa and $p_f = 5$ MPa									
V_P [m/s], 0.5 Hz, direct P-wave modulus	3958	6118	4633	3474	3060	3087	2803	2800	4649
V_P [m/s], 1 Hz, direct P-wave modulus	3974	6172	4629	3497	3111	3109	2812	2775	4655
V_P [m/s], 2 Hz, direct P-wave modulus	4004	N/A	4646	3541	3183	3150	2820	2866	4683
V_P [m/s], 250 kHz, ultrasonics	4552	6334	5105	3956	3552	3527	3275	3122	5185
V_P [m/s], 500 kHz, ultrasonics	4542	6330	5092	3953	3548	3540	3268	3114	5279
V_S [m/s], 250 kHz, ultrasonics	2308	3178	2480	2047	1837	1736	1598	1491	2675
V_P/V_S (250 kHz)	1.97	1.99	2.06	1.93	1.93	2.03	2.05	2.09	1.94
Dispersion V_P (1 Hz–250 kHz) [%]	15	3	10	13	14	13	16	14	11
Sonic log data									
V_P [m/s], 2000 Hz	4391	6067	3925	3450	3308	3131	3133	2976	5439
V_S [m/s], 2000 Hz	2224	3167	2025	1779	1786	1544	1563	1397	3099
V_P/V_S, 2000 Hz	1.97	1.92	1.94	1.94	1.85	2.03	2.00	2.13	1.76
Static data									
E [GPa], unloading conventional	21.85	68.81	31.64	16.59	11.44	12.58	9.45	9.93	42.15
E [GPa], unloading extrapolated zero-stress	25.19	69.93	37.74	18.94	13.30	14.33	10.75	10.72	48.50
$d\varepsilon_{ax}/d\sigma_{ax}$ [1/GPa], zero-stress compliance	0.040	0.014	0.027	0.053	0.075	0.070	0.093	0.093	0.021
a_{ax} [$\cdot 10^{-3}$MPa^{-2}], non-elasticity parameter	1.69	0.06	1.12	1.93	3.06	2.40	2.90	2.47	0.67
a_r [$\cdot 10^{-3}$MPa^{-2}], non-elasticity parameter	−0.35	0.05	0.14	−0.78	−0.97	−1.29	−0.99	−0.56	−0.11
E [GPa], unloading modelled at $\Delta\sigma_{ax} = 0$ MPa	25.19	69.93	37.74	18.94	13.30	14.33	10.75	10.72	48.50
E [GPa], unloading modelled at $\Delta\sigma_{ax} = 1$ MPa	24.66	69.78	36.95	18.60	13.03	14.08	10.59	10.58	47.72
E [GPa], unloading modelled at $\Delta\sigma_{ax} = 10$ MPa	20.77	68.49	31.15	16.01	11.05	12.22	9.30	9.47	41.72
PR [-], unloading modelled at $\Delta\sigma_{ax} = 0$ MPa	0.37	0.34	0.41	0.34	0.30	0.30	0.33	0.29	0.28
PR [-], unloading modelled at $\Delta\sigma_{ax} = 1$ MPa	0.36	0.33	0.40	0.34	0.30	0.30	0.33	0.29	0.28
PR [-], unloading modelled at $\Delta\sigma_{ax} = 10$ MPa	0.34	0.31	0.31	0.35	0.30	0.33	0.33	0.28	0.27
Cole–Cole model									
Difference in percent sonic logging and model fit at 20 kHz	−2	−3	−23	−12	−6	−10	−3	−3	7

Table A2. Comparison of measured ultrasonic velocities and computed stiffness parameters for the samples O2 and $O2_{TI}$ (the latter from Crisci *et al.* (2021)). For further explanations and equations of the stiffness matrix and Thomsen parameters, see Lozovyi & Bauer (2018).

Sample ID	$O2_{TI}$ aniso	$O2_{TI}$ iso	O2
Ultrasonic velocities [m/s]			
0° *P*-wave	3460	3460	3527
90° *P*-wave	4350	-	-
60° *P*-wave	3939	-	-
0° *S*-wave	1872	1872	1736
90° *S*-wave	2644	-	-
Density [g/cm^3]	2.53	2.53	2.54
Stiffness matrix [GPa]			
C_{11}	47.89	-	-
C_{33}	30.30	30.30	31.54
C_{13}	14.80	-	-
C_{44}	8.87	8.87	7.64
C_{66}	17.69	-	-
Thomsen parameters			
ε	0.29	-	-
γ	0.50	-	-
δ	0.08	-	-
Young's moduli and PRs			
E_V	23.05	22.94	20.48
E_H	39.98	-	-
E_{45}	25.02	-	-
ν_{VH}	0.25	0.29	0.34
ν_{VH}	0.43	-	-
ν_{HH}	0.13	-	-
Static data S-direction			
Pre-yield unload stress			
Range (axial) [MPa]	29–23	-	25–15
E	11	-	9.45
ν	0.31	-	0.33

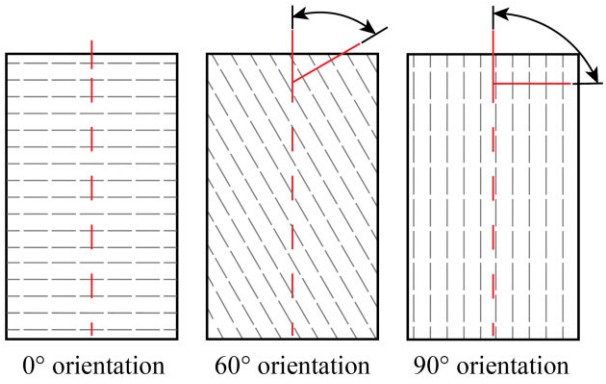

Figure A1. Core sample orientation convention.

five independent stiffness constants C_{ij} as described in Thomsen (1986). We further computed Young's modulus and Poisson's ratio in different directions. Then, we compare the latter to the isotropic assumption, using only vertical *P*- and *S*-wave velocities to calculate Young's modulus and Poisson's ratio. The difference between anisotropic and isotropic Young's moduli from ultrasonic measurements is negligible, whereas Poisson's ratio is more affected by the isotropic assumption (Table A2). The difference in ultrasonic velocities arises from a different loading and consolidation procedure (O2–stress-controlled, $O2_{TI}$–strain-controlled), as well as a difference in effective stress. It is also important to point

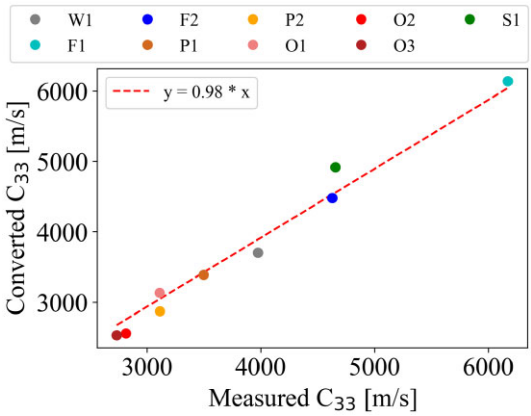

Figure A2. Converted C_{33} at 1 Hz from Young's modulus and Poisson's ratio assuming isotropy versus directly measured C_{33} *P*-wave modulus at 1 Hz ($R^2 = 0.98$). Colours indicate the nine tested samples, whereas the colour code remains the same as in all previous plots.

out that measured ultrasonic velocities with group angles deviating from TI symmetry fall between the phase and group velocity. Considering ray angle versus symmetry directions will result in phase and group velocities being nearly equal. The difference of 0.05 in Poisson's ratio is explained by a higher V_P/V_S ratio in the sample O2.

The comparison between the static triaxial unloading data shows slightly higher values for $O2_{TI}$. We explain this with higher effective stress and a lower stress range (Table A2, bottom).

We have seen that Opalinus clay exhibits anisotropic properties, but we had to make assumptions about isotropy. In order to estimate a possible error of the isotropy assumption, we compare the converted *P*-wave modulus C_{33} from Young's modulus, and Poisson's ratio measured at 1 Hz (assuming isotropy) with the measured *P*-wave modulus at 1 Hz (Fig. A2):

$$\frac{C_{33,\text{converted}}}{C_{33,\text{measured}}} = 0.98. \tag{C1}$$

It shows that $C_{33,\text{converted}}$ is about 2% smaller than $C_{33,\text{measured}}$ from direct *P*-wave modulus measurements.

APPENDIX D: COLE–COLE MODEL

The Cole–Cole relaxation model (Cole & Cole 1941) uses four fitting parameters: low- and high-frequency limit modulus, characteristic frequency f_0, which is the frequency of the attenuation peek and a parameter α, which accounts for the width of the relaxation time distribution. Cole & Cole (1941) assume only a single relaxation process of the material.

The real part of the complex modulus E' is calculated as follows:

$$E' = E_\infty + \frac{E_0 - E_\infty}{2}\left(1 - \frac{\sinh(1-\alpha)\ln\omega\tau_0}{\cosh(1-\alpha)\ln\omega\tau_0 + \cos\frac{\alpha\pi}{2}}\right) \tag{D1}$$

where E_0 and E_∞ are the low- and high-frequency Young's moduli, respectively, τ_0 is the relaxation time, ω the angular frequency and α a parameter that accounts for the width of the relaxation time distribution. The imaginary part of the complex modulus E'' follows as:

$$E'' = \frac{\frac{E_0 - E_\infty}{2}\cos\frac{\alpha\pi}{2}}{\cosh(1-\alpha)\ln\omega\tau_0 + \sin\frac{\alpha\pi}{2}}. \tag{D2}$$

APPENDIX E: MICROMECHANICAL MODEL

The micromechanical model applied in this paper considers shale a composite material with two ingredients: clay and non-clay. The model is primarily designed for understanding observed dispersion in clay-containing rocks rather than accurate predictions, as several parameters need to be estimated based on indirect empirical observations or assumptions. The model is isotropic—although shales are not. But for the shales addressed here, the full anisotropy has not been characterized, so isotropic modelling considers properties measured along the symmetry axis.

Clay is modelled following the approach by Holt & Fjær (2003) and Holt & Kolstø (2017). Solid clay minerals are embedded in a viscoelastic medium consisting of free water and bound water. All grains are covered by one or more monolayers of 'bound' (incorporating surface adsorbed) water, which is a viscoelastic substance with non-zero shear modulus. This 'effective water' can be simulated using a Voigt model, with bulk and shear moduli K_w and G_w written as

$$K_w = f_{bw}K_{bw} + (1 - f_{bw})K_{fw} \tag{E1}$$

$$G_w = f_{bw}G_{bw}, \tag{E2}$$

where subscripts bw and fw refer to bound and free water, respectively, and the volume fraction of bound water is

$$f_{bw} = N_{H_2O}\delta_{H_2O}S_g\rho_{s,cl}\frac{1-\phi_{cl}}{\phi_{cl}} + \frac{n_{H_2O}\delta_{H_2O}V_{sw}}{d_{sw}\phi_{cl}}, \tag{E3}$$

where N_{H_2O} is the number of monolayers with thickness δ_{H_2O} on the pore walls, S_g is the specific surface are, ρ_s is the solid mineral density, and ϕ_{cl} is the clay porosity. The second term represents n_{H_2O} interstitial monolayers of water inside swelling clay minerals with lattice spacing d_{sw} and V_{sw} the volume fraction of swelling minerals.

Assuming the resulting porous medium is a suspension of solid clay minerals in the effective water, the effective bulk and shear moduli of clay are given by Reuss averages:

$$\frac{1}{K_{cl}} = \frac{\phi_{cl}}{K_w} + \frac{1-\phi_{cl}}{K_{s,cl}} \tag{E4}$$

$$\frac{1}{G_{cl}} = \frac{\phi_{cl}}{G_w} + \frac{1-\phi_{cl}}{G_{s,cl}}, \tag{E5}$$

where $K_{s,\,cl}$ and $G_{s,\,cl}$ are bulk and shear moduli of the solid clay minerals.

The bound water bulk and shear moduli are key parameters in this model. Atomic force studies described in Section 1 point to viscoelastic behaviour of the bound water. Thus, we expect frequency dependence, and we anticipate that in pure clay would be no resistance to shear in the static limit. Thus, we assume that the bound water shear stiffness vanishes at zero frequency and depends only on bound water viscosity η_{bw} and an upper limit $G_{bw,\,\infty}$ at infinite frequency f. The frequency dependence may be described by a Maxwell model:

$$G_{bw} = \frac{G_{bw,\infty}}{1 + (G_{bw,\infty}/\omega\eta_{bw})^2}. \tag{E6}$$

The angular frequency $\omega = 2\pi f$. The transition frequency between low and high-frequency behaviour is hence given as

$$f_{c,bw} = \frac{G_{bw,\infty}}{2\pi\,\eta_{bw}}. \tag{E7}$$

For simplicity, we neglect dispersion in the bulk modulus of bound water and assume that K_{bw} has a value close to the bulk modulus of free water. In our analysis, we use the observed enhanced viscosity for the innermost monolayer (Zhu & Granick 2001) and limit the bound water to one molecular layer, and use laboratory-measured ultrasonic velocities as guidelines to select $G_{bw,\,\infty}$.

The *non-clay* medium is thought of as a cemented porous material with solid moduli estimated as the Voigt average. The calculated non-clay porosity $\phi_{non\text{-}cl}$ ensures that the total porosity ϕ agrees with laboratory-measured porosity.

$$\phi_{non\text{-}cl} = \frac{\phi - \nu_{cl}\phi_{cl}}{\nu_{cl}}, \tag{E8}$$

$$\nu_{cl} = \frac{V_{cl}}{V}. \tag{E9}$$

The solid moduli are used to estimate the drained (framework) moduli. For simplicity, we choose to build on a critical porosity model that expresses softening by porosity (Nur *et al.* 1998; Fjær *et al.* 2021).

$$K_{fr,non\text{-}cl} = K_{s,non\text{-}cl}\left(1 - \frac{\phi_{non\text{-}cl}}{\phi_{cr}}\right) \tag{E10}$$

$$G_{fr,non\text{-}cl} = G_{s,non\text{-}cl}\left(1 - \frac{\phi_{non\text{-}cl}}{\phi_{cr}}\right) \tag{E11}$$

Here ϕ_{cr} is the critical porosity, which is well above the porosities of the non-clay fraction in the samples studied here, so the frame moduli of non-clay are marginally smaller than their solid grain moduli.

The non-clay component is assumed to be fully saturated with free water, while the clay component, which dominates the specific surface area, contributes the main part of the bound water content. Free water saturation is added by the Gassmann equation in the low frequency limit (Gassmann 1951):

$$K_{sat,non\text{-}cl} = K_{fr,non\text{-}cl} + \alpha^2_{non\text{-}cl}M_{non\text{-}cl} \tag{E12}$$

$$G_{sat,non\text{-}cl} = G_{fr,non\text{-}cl} \tag{E13}$$

Here the non-clay Biot coefficient is

$$\alpha_{non\text{-}cl} = 1 - \frac{K_{fr,non\text{-}cl}}{K_{s,non\text{-}cl}} \tag{E14}$$

and the inverse of Biot's storage modulus is

$$\frac{1}{M_{non\text{-}cl}} = \frac{\phi_{non\text{-}cl}}{K_{fr}} + \frac{\alpha_{non\text{-}cl} - \phi_{non\text{-}cl}}{K_{s,non\text{-}cl}}. \tag{E15}$$

The saturated Gassmann material is thought of as host material for microcracks. These can be cracks formed by mechanical stresses or can be associated with asperities in grain contact areas. Such cracks are less likely to occur in clay since pure clay acts as a suspension. Mathematically, microcracks are added as introduced by Budiansky & O'connell (1976) and outlined by Fjær *et al.* (2021).

$$K_{non\text{-}cl} = K_{sat,non\text{-}cl}\left(1 - \frac{16(1-\nu^2_{s,non\text{-}cl})}{9(1-2\nu_{s,non\text{-}cl})}D_c\xi_{non\text{-}cl}\right) \tag{E16}$$

$$G_{non\text{-}cl} = G_{sat,non\text{-}cl}\left(1 - \frac{32(1-\nu_{s,non\text{-}cl})}{45}\left(D_c + \frac{3}{2-\nu_{s,non\text{-}cl}}\right)\xi_{non\text{-}cl}\right), \tag{E17}$$

where $\xi_{non\text{-}cl}$ is crack density in the non-clay. D_c controls the squirt flow of water between cracks (soft pores) and (stiff) pores. In the low-frequency limit, $D_c \to 1$, whereas $D_c \to 0$ at infinite frequency. The intermediate behaviour is frequency dependent, showing a transition from low to high-frequency behaviour at

$$f_{c,sqrt} \approx \frac{\gamma^3_{asp.rat}K_{sat,non\text{-}cl}}{\eta_{fw}}, \tag{E18}$$

Table E1. Input parameters for the micromechanical model and guidelines for allocating values.

Eq.	Parameter	Value	Guideline
E1	K_{fw}	2.5 GPa	Free water modulus depends on temperature, salinity and pressure (see Mavko *et al.* 2009).
E1	K_{bw}	2.5 GPa	Bound water bulk modulus assumed same as K_{fw}.
E3	$N_{\mathrm{H_2O}}$	1	Number of molecular layers of bound water on solid mineral surfaces.
E3	$n_{\mathrm{H_2O}}$	1	Number of molecular of bound water interstitially in swelling clay (here smectite).
E3	$\delta_{\mathrm{H_2O}}$	0.25 nm	Size of water molecule on the pore walls.
E3	S_g	measured	Specific surface area (predominantly clay) in $\mathrm{m^2\ g^{-1}}$.
E3	$\rho_{\mathrm{s,cl}}$	2.79 g/ cm	Density of solid phase in clay; number chosen is for muscovite (Fjær *et al.* 2021).
E3	ϕ_{cl}	0.13	Porosity of clay; value as given by Mazurek *et al.* (2023) for Opalinus clay.
E3	d_{sw}	1.21 nm	Lattice spacing of swelling clay mineral, here selected as for basic spacing of smectite (Colten-Bradley 1987; Hüpers & Kopf 2012).
E4,E5	$K_{\mathrm{s,\,cl}}$ and $G_{\mathrm{s,\,cl}}$	54 and 36 GPa	Bulk and shear moduli for pure clay mineral; chosen values represent muscovite (e.g. Fjær *et al.* 2021).
E6	$G_{\mathrm{bw},\,\infty}$	1.5 GPa	Bound water shear modulus at infinite frequency, varies from 0.5 to 3 GPa. May be tuned by matching ultrasonic data to model predictions.
E6	η_{bw}	$\leq 10^6$ Pa · s	Viscosity of bound water. Here chosen as representative for the monolayer closest to the mineral surface as seen in atomic force studies by Zhu & Granick (2001), but will, in general, be heterogeneous and decrease strongly for each additional monolayer away from the surface.
E10, E11	ϕ_{cr}	0.4	Critical porosity for non-clay (Nur *et al.* 1998).
E16, E17	$\xi_{\mathrm{non\text{-}cl}}$	Adjustable	Crack density in non-clay varies from 0 to 0.2, here 0.15.
E18	$\gamma^3_{\mathrm{asp.rat}}$	Adjustable	Aspect ratio in cracks in non-clay, varies from 10^{-3} to 10^{-1}, here 0.005.
E18	η_{fw}	10^{-3} Pa · s	Viscosity of fee water.

where $\gamma_{\mathrm{asp.rat}}$ is the aspect ratio of microcracks, and we consider the surrounding Gassmann material as equivalent to the solid surrounding material in O'Connell & Budiansky (1977). η_{fw} is free water viscosity (10^{-3}Pa · s).

The properties of the *composite shale* are finally computed by deriving the Voigt and Reuss averages of the elastic stiffnesses of the ingredients:

$$K_V = \nu_{\mathrm{cl}} K_{\mathrm{cl}} + (1-\nu_{\mathrm{cl}}) K_{\mathrm{non\text{-}cl}} \tag{E19}$$

$$\frac{1}{K_R} = \frac{\nu_{\mathrm{cl}}}{K_{\mathrm{cl}}} + \frac{1-\nu_{\mathrm{cl}}}{K_{\mathrm{non\text{-}cl}}} \tag{E20}$$

$$G_V = \nu_{\mathrm{cl}} G_{\mathrm{cl}} + (1-\nu_{\mathrm{cl}}) G_{\mathrm{non\text{-}cl}} \tag{E21}$$

$$\frac{1}{G_R} = \frac{\nu_{\mathrm{cl}}}{G_{\mathrm{cl}}} + \frac{1-\nu_{\mathrm{cl}}}{G_{\mathrm{non\text{-}cl}}}. \tag{E22}$$

The most realistic value in such averaging schemes is somewhere between the upper Voigt and the lower Reuss bound, often chosen as the Voigt–Reuss–Hill (VRH) value, which is simply the average of the Voigt and Reuss moduli. However, with a clay-dominated shale, the true answer is likely to be closer to clay than non-clay and vice versa. Hence, we use a volume-weighted average of Reuss and Hill bounds (weighted VRH) instead of the more common VRH:

$$K_{\mathrm{VRH_w}} = \nu_{\mathrm{cl}} K_R + (1-\nu_{\mathrm{cl}}) K_V \tag{E23}$$

$$G_{\mathrm{VRH_w}} = \nu_{\mathrm{cl}} G_R + (1-\nu_{\mathrm{cl}}) G_V. \tag{E24}$$